

## Collisional depolarisation in electronically excited radicals

H. Chadwick<sup>a†</sup>, M. Brouard<sup>a\*</sup>, T. Perkins<sup>a</sup> and F. J. Aoiz<sup>b</sup>

<sup>a</sup>*The Department of Chemistry, University of Oxford, The Physical and Theoretical Chemistry Laboratory, South Parks Road, Oxford, OX1 3QZ, United Kingdom;*

<sup>b</sup>*Departamento de Química Física, Facultad de Química, Universidad Complutense, 28040 Madrid, Spain*

(January 2014)

Recent work on collisional depolarisation in electronically excited radicals is reviewed, with a focus on the NO(A) and OH(A) radicals in collisions with rare gas atoms. The mechanism of depolarisation, and its competition with other collisional processes, is investigated using a combination of experimental and theoretical methods. The present state of the field is also put into context with other, related work in similar areas.

**Keywords:** Potential energy surface; depolarisation; angular momentum; inelastic collisions; alignment; orientation

### Contents

|  | PAGE |
|--|------|
| 1. Introduction                        | 3    |
| 2. Summary of depolarisation formalism | 6    |

---

<sup>†</sup>Current address: Laboratoire de Chimie Physique Moléculaire, Ecole Polytechnique Fédérale de Lausanne, Switzerland

\*Corresponding author. Email: mark.brouard@chem.ox.ac.uk

|   |    |
|---|----|
| 2.1. Notation   | 6  |
| 2.2. Opacity functions and cross sections                     | 7  |
| 2.3. Angular momentum polarisation                            | 8  |
| 2.4. Angular momentum depolarisation                          | 10 |
| 2.5. Tensor opacities and quasi-open shell QCT                | 12 |
| <b>3. Methods</b>   | 13 |
| 3.1. Comparison of experimental methods                       | 13 |
| 3.2. Quantum beat spectroscopy                                | 15 |
| 3.2.1. Zeeman beats   | 17 |
| 3.2.2. Total depolarisation measurements                      | 17 |
| 3.2.3. Elastic depolarisation measurements                    | 19 |
| 3.2.4. Hyperfine beats  | 19 |
| 3.2.5. Translational moderation of OH(A)                      | 20 |
| 3.3. Theoretical methods                                      | 21 |
| 3.3.1. QM method  | 21 |
| 3.3.2. QCT method   | 22 |
| 3.3.3. TSH-QCT method   | 24 |
| <b>4. Depolarisation in triatomic systems</b>                 | 25 |
| 4.1. QM vs QCT calculations for OH(A) + Rg and NO(A) + Rg     | 25 |
| 4.2. Rotational energy transfer for OH(A) + Rg and NO(A) + Rg | 27 |
| 4.3. Total (elastic + inelastic) depolarisation               | 31 |
| 4.3.1. NO(A) + Rg, 300 K                                      | 31 |
| 4.3.2. OH(A) + Rg, 300 K                                      | 33 |

|  |    |
|--|----|
| <i>International Reviews in Physical Chemistry</i>                       | 3  |
| 4.3.3. $\text{NO(A)} + \text{Rg}$ vs $\text{OH(A)} + \text{Rg}$ , 300 K  | 34 |
| 4.3.4. Superthermal $\text{OH(A)} + \text{Rg}$                           | 35 |
| 4.4. Elastic depolarisation of $\text{OH(A)} + \text{Rg}$ , 300 K        | 37 |
| 4.5. Inelastic depolarisation of $\text{OH(A)} + \text{Rg}$ , 300 K      | 40 |
| 4.6. Non-adiabatic effects in $\text{OH(A)} + \text{Kr}$                 | 42 |
| 4.7. Comparison to $\text{CN(A)} + \text{Ar}$                            | 44 |
| 4.8. Crossed-beam studies of $\text{NO(A)} + \text{Rg}$                  | 46 |
| <b>5. Mechanism of depolarisation</b>                                    | 48 |
| 5.1. Kinematic apse  | 48 |
| 5.2. Deflection functions ( $b$ vs $\theta$ )                            | 50 |
| 5.3. Opacity functions   | 51 |
| 5.4. TSH-QCT opacity functions   | 52 |
| <b>6. Depolarisation in larger systems</b>                               | 53 |
| 6.1. $\text{NO(A)} + \text{N}_2$ and $\text{NO(A)} + \text{O}_2$ , 300 K | 53 |
| 6.2. $\text{OH(A)} + \text{H}_2$ , 300 K                                 | 55 |
| <b>7. Conclusions and future work</b>                                    | 56 |

## 1. Introduction

The depolarisation of angular momentum of open shell radicals in collisions with small molecules has been a topic of considerable interest in recent years [1–27]. As a measurement of the  $\mathbf{j} - \mathbf{j}'$  correlation, collisional depolarisation gives an insight into the dynamics of rotationally elastic and inelastic collisions that is complemen-

tary to that available from scalar properties. In addition, depolarisation properties are exquisitely dependent on the attractive or repulsive character of the interaction, providing a deeper understanding of the nature of the collision mechanism.

Recent reviews of this field by Paterson *et al.* [23, 24] have detailed the various kinetic formalisms and experimental techniques used to investigate collisional depolarisation, and compared theoretical scattering of  $\text{OH}(\text{X}^2\Pi)$  and  $\text{NO}(\text{X}^2\Pi)$  with He and Ar. Scattering of the excited state radicals  $\text{NO}(\text{A}^2\Sigma^+)$  and  $\text{OH}(\text{A}^2\Sigma^+)$  was treated in those reviews as a comparison to the main focus, which is the ground state dynamics. Therefore, in this work, we focus on the collisions of electronically excited radicals – principally  $\text{NO}(\text{A}^2\Sigma^+)$  and  $\text{OH}(\text{A}^2\Sigma^+)$  – with rare gas atoms, comparing the extent and mechanisms of depolarisation in each with the use of experimental and theoretical data.

We choose  $\text{NO}(\text{A}) + \text{Rg}$  and  $\text{OH}(\text{A}) + \text{Rg}$  because of their theoretical tractability – accurate *ab initio* PESs have been calculated for many such systems [5, 22, 28, 29]. For this reason, these radicals have been very widely studied, and serve as prototypes for the scattering of atoms with open shell diatoms. In addition, the NO and OH radicals have very different kinematics, with OH having its centre of mass close to one end of the radical while, in NO, the centre of mass is much more central. The potential energy surfaces also range from the almost purely repulsive, very isotropic  $\text{NO}(\text{A}) + \text{He}$  system right the way to the highly anisotropic  $\text{OH}(\text{A}) + \text{Kr}$  system, which features a potential well of  $\approx 6000 \text{ cm}^{-1}$ . In this way, the effects of kinematics and of the PES can both be investigated.

A secondary focus of this review is on the interplay between electronically adiabatic

(RET, rotationally elastic and inelastic depolarisation) and non-adiabatic (quenching) processes in systems such as  $\text{OH}(\text{A}) + \text{Kr}$  that display significant electronic quenching. This has been explored in several recent papers [26, 27, 30], and informs similar studies with larger molecules, for example  $\text{H}_2$  [31, 32]. Analysis of collisions where the products remain on the excited PES can provide information about which kinds of collisions do, and do not, lead to quenching or reactive outcomes.

In section 2, we will first summarise the quantities measured and discussed in this review. Section 3 will set out the experimental and theoretical methods used to obtain most of the results presented here. Results will be presented in section 4 for rotational energy transfer and depolarisation in both rotationally elastic and inelastic collisions, and the effects of the electronically non-adiabatic channel in  $\text{OH}(\text{A}) + \text{Kr}$  will be examined in section 4.6. Recent work performed on the  $\text{CN}(\text{A}) + \text{Ar}$  system, and molecular beam studies of  $\text{NO}(\text{A}) + \text{Rg}$ , will also be summarised for comparison with the present results. Section 5 contains a deeper investigation into the mechanisms of depolarisation in the systems considered here, using theoretical methods to probe the different behaviours observed. Collisions of  $\text{OH}(\text{A})$  and  $\text{NO}(\text{A})$  with diatomic colliders are considered in section 6. Adding a fourth atom makes theoretical comparisons much more difficult than in the atom-diatom case, so these experimental results are considered in comparison to the  $\text{OH}(\text{A}) + \text{Rg}$  and  $\text{NO}(\text{A}) + \text{Rg}$  systems already summarised. Finally, section 7 summarises the conclusions of this work.

## 2. Summary of depolarisation formalism

### 2.1. Notation

Here we employ the following notation [5, 13, 14, 16, 17, 20–22].  $\mathbf{N}$  ( $\mathbf{N}'$ ) denotes the diatomic rotational angular momentum apart from electron and nuclear spin. For a diatomic radical in a  $^2\Sigma^+$  electronic state, for which electronic orbital angular momentum is zero,  $\mathbf{N}$  ( $\mathbf{N}'$ ) is equivalent to the nuclear rotational angular momentum, which must lie perpendicular to the internuclear axis,  $\mathbf{r}$ . The corresponding quantum number is written  $N$  ( $N'$ ). The total rotational angular momentum apart from nuclear spin of OH(A) and NO(A) is denoted by  $\mathbf{j}$ , and its quantum number as  $j$ . In the Hund's case (b) coupling scheme appropriate for  $^2\Sigma^+$  radicals, the molecular wave function is defined by  $\mathbf{j} = \mathbf{N} + \mathbf{S}$ , where  $\mathbf{S}$  is the electronic spin. For every  $N$  state (except for  $N = 0$ ), there will be two possible  $j$  values,  $j = N + 1/2$  and  $j = N - 1/2$ , which are denoted  $f_1$  and  $f_2$  states, respectively. The reactant and product quantum numbers  $F$  and  $F'$  are associated with the total diatomic angular momentum, including both electron and nuclear spin, *i.e.*  $\mathbf{F} = \mathbf{j} + \mathbf{I}$ . The orbital angular momentum of the triatomic system is labelled  $\ell$  ( $\ell'$ ). The total angular momentum quantum number of the collision system is denoted by  $J$  and its projection onto the space fixed  $Z$ -axis by  $M_J$ .

## 2.2. Opacity functions and cross sections

The inelastic probability of a transition between initial  $|i\rangle$  and final  $|f\rangle$  electronic-rovibrational states as a function of the total angular momentum,  $J$ , is given by

$$P_{if}(J) = \frac{1}{2\min(J, j) + 1} \sum_{\ell=|J-j|}^{J+j} \sum_{\ell'} |T_{f\ell', i\ell}^J|^2 \quad (1)$$

where  $\ell$  and  $\ell'$  are the initial and final orbital angular momentum and  $j$  is the initial rotational angular momentum.  $T_{f\ell', i\ell}^J$  represents the element of the transition matrix  $\mathbf{T} = \mathbf{1} - \mathbf{S}$ , where  $\mathbf{S}$  is the scattering matrix.

The analogous probability as a function of the orbital angular momentum, that is the opacity function, can be written as [33]:

$$P_{if}(\ell) = \frac{1}{(2\ell + 1)(2j + 1)} \sum_{J=|\ell-j|}^{\ell+j} \sum_{\ell'} (2J + 1) |T_{f\ell', i\ell}^J|^2 \quad (2)$$

For  $J \gg j$  for which  $J \sim \ell$ , both probabilities converge to the same values. Usually, the inelastic probability,  $P_{if}(J)$ , is also called the opacity function, although rigorously speaking this term would have to be reserved for the probability as a function of the orbital angular momentum.

The classical opacity function in terms of the real valued impact parameter,  $b$ , can be written as

$$P_{if}(b) = \frac{\mathcal{N}_{if}(b)}{\mathcal{N}_i(b)}, \quad (3)$$

where  $\mathcal{N}_{if}(b)$  are the number of trajectories out of  $\mathcal{N}_i(b)$  that have undergone the  $|i\rangle \rightarrow |f\rangle$  transition within the infinitesimal range of impact parameters  $[b, b+db]$ . The opacity function can also be expressed in terms of the orbital angular momentum,  $\ell$ , with the equivalence  $b = [\ell(\ell + 1)]^{1/2}/k_i$ , where  $k_i = \mu v_r/\hbar$  is the initial relative wavenumber of the collision,  $\mu$  the relative reduced mass and  $v_r$  the relative velocity.

The  $J$ -partial cross section at a given collision energy,  $E_{\text{coll}}$ , can be written as

$$\sigma_{if}^J(E_{\text{coll}}) = \frac{\pi}{k_i^2} \frac{2J+1}{2j+1} [2 \min(J, j) + 1] P_{if}(J) \quad (4)$$

The integral cross section is then given by

$$\sigma_{if}(E_{\text{coll}}) = \frac{\pi}{k_i^2} \frac{1}{2j+1} \sum_J (2J+1) [2 \min(J, j) + 1] P_{if}(J) \quad (5)$$

The classical expression is given by [33]

$$\sigma_{if}(E_{\text{coll}}) = \frac{\pi}{k_i^2} \int_0^{\ell_{\text{max}}} (2\ell+1) P_{if}(\ell) d\ell = 2\pi \int_0^{b_{\text{max}}} b P_{if}(b) db \quad (6)$$

If the sampling in  $b$  is uniform in  $b^2$  (or  $\ell$  in  $\ell(\ell+1)$ )

$$\mathcal{N}_i(\ell) = \frac{(2\ell+1)}{[\ell_{\text{max}}(\ell_{\text{max}}+1)]} \mathcal{N}_i \quad \text{or} \quad (7)$$

$$\mathcal{N}_i(b) = \frac{2b}{b_{\text{max}}^2} \mathcal{N}_i \quad (8)$$

where  $\mathcal{N}_i$  is the total number of trajectories starting in the  $|i\rangle$  state. Substituting in the classical expression of  $P_{if}(b)$  and in Eq. (6)

$$\sigma_{if}(E_{\text{coll}}) = \pi b_{\text{max}}^2 \frac{\mathcal{N}_{if}}{\mathcal{N}_i} = \frac{\pi}{k_i^2} [\ell_{\text{max}}(\ell_{\text{max}}+1)] \frac{\mathcal{N}_{if}}{\mathcal{N}_i} \quad (9)$$

where  $\mathcal{N}_{if}$  is the total number of trajectories that have experienced the  $|i\rangle \rightarrow |f\rangle$  transition.

Notice that the latter expressions, commonly used, are only valid as long as  $b$  or  $\ell$  are uniformly sampled in  $b^2$  or in  $\ell(\ell+1)$ .

### 2.3. Angular momentum polarisation

The classical probability density function,  $P(\theta_j, \phi_j)$ , gives the probability of  $\mathbf{j}$  pointing in the direction  $(\theta_j, \phi_j)$  with respect to the scattering frame whose  $z$  axis is defined by the initial relative velocity,  $\mathbf{k}$ , and where the  $\phi = 0$  plane is defined by the  $\mathbf{k} - \mathbf{k}'$  plane. This function can be expanded in the complex conjugates of modified spherical



harmonics [34, 35]:

$$P(\theta_j, \phi_j) = \sum_{k=0}^{\infty} \sum_{q=-k}^k \frac{2k+1}{4\pi} a_q^{(k)} C_{kq}^*(\theta_j, \phi_j) \quad (10)$$

The expansion coefficients,  $a_q^{(k)}$ , are given by

$$a_q^{(k)} = \langle C_{kq}(\theta_j, \phi_j) \rangle \quad (11)$$

In the quantum description, the direction of  $\mathbf{j}$  cannot be precisely defined, and so the density matrix is expanded in Clebsch-Gordan coefficients [34, 35]:

$$\langle jm|\rho|jm'\rangle = \sum_{k=0}^{2j} \sum_{q=-k}^k \frac{2k+1}{2j+1} a_q^{(k)} \langle jm, kq|jm'\rangle \quad (12)$$

In this expansion, the  $a_q^{(k)}$  polarisation parameters are given by

$$a_q^{(k)} = \sum_{mm'} \langle jm|\rho|jm'\rangle \langle jm, kq|jm'\rangle \quad (13)$$

In order to link the quantum and classical descriptions, it is possible to define a quantum probability density function  $Q(\theta_j, \phi_j)$  that describes the population of the minimum uncertainty state [34, 35].

$$Q(\theta_j, \phi_j) = \sum_{k=0}^{2j} \sum_{q=-k}^k \frac{2k+1}{4\pi} a_q^{(k)} \langle jj, k0|jj\rangle C_{kq}^*(\theta_j, \phi_j) \quad (14)$$

In the limit of high  $j$ , the Clebsch-Gordan coefficient tends to unity, leading to a correspondence between equations (14) and (10).

In a cylindrically symmetric collision system,  $q = 0$  and the spherical harmonics become Legendre polynomials. The classical polarisation parameters are

$$a_0^{(k)} = \langle P_k(\cos \theta_j) \rangle \quad (15)$$

The odd- $k$  moments describe the orientation of the sample (classically, a preferred sense of rotation) and the even- $k$  moments describe alignment (a preferred plane of rotation). Quantum mechanically, orientation corresponds to a preference for positive over negative values of  $m_j$  (or vice versa), and alignment to a preferential population

of high over low (or low over high)  $m_j$  states.

## 2.4. Angular momentum depolarisation

Collisional depolarisation of angular momentum is described by the correlation between  $\mathbf{j}$  and  $\mathbf{j}'$ . For the time being we will not make a distinction between  $\mathbf{j}$  and  $\mathbf{N}$  (or  $\mathbf{j}'$  and  $\mathbf{N}'$ ), neglecting the role of the electronic spin, and we will write our equations in terms of  $N$  and  $N'$  [13, 21].

Given cylindrical symmetry, the classical  $\mathbf{N}$ – $\mathbf{N}'$  vector correlation can be written as an expansion in Legendre polynomials:

$$P(\theta_{NN'}) = \sum_k \frac{2k+1}{2} a^{(k)}(N, N') P_k(\cos \theta_{NN'}) \quad (16)$$

where  $\theta_{NN'}$  is the angle between  $\mathbf{N}$  and  $\mathbf{N}'$ . The coefficients of the expansion,  $a^{(k)}(N, N')$ , are the depolarisation moments, which can be calculated as

$$a^{(k)}(N, N') = \langle P_k(\theta_{NN'}) \rangle = \frac{1}{\mathcal{N}_{NN'}} \sum_{i=1}^{\mathcal{N}_{NN'}} P_k(\cos \theta_{NN'}^{(i)}) \quad (17)$$

where  $\mathcal{N}_{NN'}$  is the number of trajectories out of all those starting in  $|N\rangle$ ,  $\mathcal{N}_N$ , that undergo the  $|N\rangle \rightarrow |N'\rangle$  transition and  $\theta_{NN'}^{(i)}$  is the angle between  $\mathbf{N}$  and  $\mathbf{N}'$  for the  $i^{\text{th}}$  trajectory. The depolarisation moments are a measure of the transfer of polarisation from the initial to the final state, with the odd- $k$  moments dealing with transfer of orientation and the even- $k$  moments with transfer of alignment.

The classical RET integral cross section for  $|N\rangle \rightarrow |N'\rangle$  transition can be calculated

$$\sigma_{N,N'} = \pi b_{\text{max}}^2 \frac{\mathcal{N}_{NN'}}{\mathcal{N}_N} \quad (18)$$

These quantities can be linked to each other through the definition of tensor cross sections,  $\sigma_{\text{T}}^{(k)}(N, N')$  which quantify how much polarisation is conserved in scattering

from  $N$  to  $N'$ :

$$\sigma_{\text{T}}^{(k)}(N, N') = a^{(k)}(N, N')\sigma_{N, N'} = \frac{\pi b_{\text{max}}^2}{\mathcal{N}_N} \sum_{i=1}^{\mathcal{N}_{NN'}} P_k(\cos \theta_{NN'}^{(i)}) \quad (19)$$

such that  $\sigma_{\text{T}}^{(0)}(N, N') = \sigma_{N, N'}$ .

The quantum mechanical tensor cross sections are given by Alexander and Davis [36] and discussed by Alexander and Dagdigian [10–12]

$$\sigma_T^{(k)}(N, N') = \frac{\pi}{k_i^2} \sum_{JJ'} \sum_{\ell\ell'} (2J+1)(2J'+1)(-1)^{\ell+\ell'-N-N'+2J} \left\{ \begin{matrix} N & N & k \\ J & J' & \ell \end{matrix} \right\} \left\{ \begin{matrix} N' & N' & k \\ J & J' & \ell' \end{matrix} \right\} T_{N'\ell'N\ell}^J T_{N'\ell'N\ell}^{J*} \quad (20)$$

As discussed in reference [23], the depolarisation moments (or multipole transfer coefficients),  $a^{(k)}(j, j')$ , are the same as the multipole transfer efficiencies  $E^{(k)}(j, j')$  of Alexander and Orlikowski[40]. Further links between different formalisms are reviewed in reference [23].

The collisional depolarisation cross-section,  $\sigma_{N, N'}^{(k)}$ , describes the loss of polarisation in scattering from  $|N\rangle$  to  $|N'\rangle$ , and can be written as [10–14, 21, 23]

$$\sigma_{N, N'}^{(k)} = \sigma_{N, N'} - \sigma_{\text{T}}^{(k)}(N, N') = \sigma_{N, N'}[1 - a^{(k)}(N, N')] \quad (21)$$

Hereinafter, ‘elastic’ collisional depolarisation refers to  $\sigma_{j, j'}^{(k)}$ , and inelastic depolarisation is  $\sigma_{\text{inel}}^{(k)} = \sum_{j'} \sigma_{j, j'}^{(k)}$  summed over all possible final  $j'$  states with  $j \neq j'$ . ‘Total’ collisional depolarisation is the sum of inelastic and elastic collisional depolarisation.

However, in the case where electronic spin is neglected and  $N$  and  $j$  are taken as equivalent, inelastic collisional depolarisation refers to  $\sigma_{\text{inel}}^{(k)} = \sum_{N'} \sigma_{N, N'}^{(k)}$  summed over all possible final  $N'$  states with  $N \neq N'$ , and elastic depolarisation refers to  $\sigma_{N, N}^{(k)}$ . If the electronic spin is taken into account either in the QCT or QM treatments, the states  $j$  and  $j'$  must replace  $N$  and  $N'$  in all the equations of this section.

In the rest of this review, the terms ‘elastic’ and ‘inelastic’ have their open shell ( $j$ ) meanings unless otherwise stated. The depolarisation moments for total (elastic plus inelastic) depolarisation will be expressed simply as  $a^{(k)}$ , meaning that [14]

$$\sigma^{(k)} = \sigma_N [1 - a^{(k)}] \quad (22)$$

## 2.5. Tensor opacities and quasi-open shell QCT

In the previous subsection, the electronic spin  $\mathbf{S}$  of the open shell radicals OH(A) and NO(A) was neglected, but both are doublet radicals with  $S = 0.5$ . The equations in section 2.4 can be modified to the open shell case by replacing  $N$  and  $N'$  with  $j$  and  $j'$ .

For collisions of a  $^2\Sigma^+$  radical with a rare gas atom, the potential is electrostatic in nature, and so it is a good assumption to treat spin as a spectator in the collisions. This corresponds to the energy-sudden limit, where the spin-rotation constant  $\gamma$  does not change on formation of the collision complex. It has been shown that the integral (RET) cross-section  $\sigma_{jj'}$  can be factorised, under this assumption, into a geometrical term that accounts for angular momentum coupling and a *tensor opacity* term,  $P^K(N, N')$ , that contains all the dynamical information about the collision [13, 36–39].  $\mathbf{K} = \mathbf{N}' - \mathbf{N}$  here is the angular momentum transfer vector.

$$\sigma_{jj'} = \frac{\pi}{k_i^2} (2j' + 1) \sum_K \left\{ \begin{matrix} N & N' & K \\ j' & j & S \end{matrix} \right\}^2 P^K(N, N') \quad (23)$$

As the tensor opacity is independent of spin, it can be calculated by quantum mechanical *or* QCT methods, thus providing a way to obtain quasi open shell cross sections from QCT calculations. The quantum mechanical definition of  $P^K(N, N')$  is

[36, 37, 39]

$$P^K(N, N') = \frac{1}{2K+1} \sum_{\ell\ell'} |\langle N'\ell' || T^K || N\ell \rangle|^2 \quad (24)$$

where

$$\langle N'\ell' || T^K || N\ell \rangle = (2K+1)(-1)^{N+\ell'} \sum_J (-1)^J (2J+1) \left\{ \begin{matrix} N & N' & K \\ \ell & \ell' & J \end{matrix} \right\} T_{N'\ell', N\ell}^J \quad (25)$$

References [13, 21] show that the tensor opacities can be calculated classically *via*

$$P^K(N, N') = \frac{k_i^2}{\pi} (2N+1) \sigma_{NN'}(K) \quad (26)$$

The  $K$ -resolved cross sections can be calculated from QCT data *via* [13]

$$\sigma_{NN'}(K) = \pi b_{\max}^2 \frac{\mathcal{N}(K; N, N')}{\mathcal{N}_{\text{tot}}(N)} \quad (27)$$

where  $\mathcal{N}(K; N, N')$  trajectories out of  $\mathcal{N}_{\text{tot}}(N)$  starting in rotational state  $N$  end up in rotational state  $N'$  after transferring  $K$  units of angular momentum. The tensor opacities are used in equation (23) to obtain the quasi open shell  $\sigma_{jj'}$ , and the calculation of quasi open shell polarisation parameters  $a^{(k)}(j, j')$  is dealt with as in references [13, 21].

Note that, as the spectator assumption is even more valid for nuclear spin than for electron spin, this can be included in the same way as described in references [13, 21].

### 3. Methods

#### 3.1. Comparison of experimental methods

The various methods of measuring experimental cross sections for collisional depolarisation have been extensively compared in reference [23], and so will be summarised only briefly here.

Excited states can be probed by polarised one-photon laser-induced fluorescence

(LIF) spectroscopy, with the fluorescence being detected in a polarisation-sensitive manner. For the measurement of collisional disalignment, a linear polarised pump laser is used to create an aligned sample of excited state molecules, with the use of two experimental geometries in which the laser polarisation and detected polarisation directions are parallel ( $\parallel$ ) and perpendicular ( $\perp$ ). The weighted sum of fluorescence intensities from the two geometries,  $I_{\parallel} + 2I_{\perp}$ , depends only on the excited state population and not on the alignment, and the difference  $I_{\parallel} - I_{\perp}$  is a measure of the alignment. The normalised difference  $P$  can therefore be used as a measure of polarisation:

$$P = \frac{I_{\parallel} - I_{\perp}}{I_{\parallel} + 2I_{\perp}} \quad (28)$$

The decay in polarisation can be measured at various collider pressures to obtain a rate constant for collisional disalignment. In the measurement of disorientation, left and right handed circularly polarised light is used, with the polarisation ratio being given by the normalised difference  $C$ :

$$C = \frac{I_L - I_R}{I_L + I_R} \quad (29)$$

This ratio does still contain a small contribution from alignment, but, in practice, this is usually within experimental error. An extension of the one-photon LIF method is quantum beat spectroscopy, which is the technique used in this work and will be described further in the following subsections.

Using two lasers in an optical-optical double resonance (OODR) or  $1 + 1'$  LIF technique can give extra rotational state resolution compared to the one-photon LIF method, for which the fluorescence must be dispersed to gain such resolution. Costen

*et al.* [18, 25] have recently used a variant of OODR on CN(A) in which the probe laser is tuned to stimulated emission on the  $A \leftarrow X$  band. In their experiments, the probe laser is frequency modulated, giving greater sensitivity.

Non-linear spectroscopic techniques such as four-wave mixing or polarisation spectroscopy (PS) have the advantage of being applicable to almost any arrangement of electronic states. In particular, PS has been used to measure collisional depolarisation in the ground state radicals OH(X) and NO(X), as reviewed in reference [24]. However, PS is a measure of bulk polarisation, and cannot separate out the effects from loss of population and loss of polarisation in the way that the one-photon LIF or OODR techniques can.

### 3.2. Quantum beat spectroscopy

The experimental procedures for determining depolarisation cross sections from quantum beat spectroscopy have been described previously [3, 14, 16, 17, 21] and only a brief summary will be given here. Translationally excited, superthermal OH(X) was generated by pulsed 193 nm photodissociation of hydrogen peroxide [40–48]. OH(X) was excited to the A state using the  $A^2\Sigma^+ \leftarrow X^2\Pi$  transition. For the thermal measurements, a time delay sufficient to allow for full translational thermalisation was used (9  $\mu$ s); ‘superthermal’ measurements were performed at shorter photolysis-probe delay times (see section 3.5). The experiments on the depolarisation of NO(A) were conducted in a slow flow of NO(X). NO(A) was produced in  $f_2$  ( $j = N - 0.5$ ) spin-rotation levels by excitation on the (0,0) band of the NO  $A \leftarrow X$  transition. The spontaneous  $A \rightarrow X$  fluorescence was passed through a set of polarising optics (see be-

low) before being detected with a UV-sensitive photomultiplier. In all experiments, the collider gas flowed into the chamber through a separate inlet valve to allow experiments to be performed over a range of partial pressures.

In the case of alignment measurements, a Glan-Taylor polariser and photoelastic modulator were used to switch the probe laser linear polarisation either perpendicular to the fluorescence detection direction or parallel to it on alternate laser shots. The polariser used for detection was aligned parallel to the probe laser propagation axis. In the case of orientation measurements, the probe radiation was switched between left and right circularly polarised light on alternate laser shots using a photoelastic modulator. A quarter waveplate followed by a Glan-Taylor polariser were placed in front of the entrance slits of the monochromator.

In the total alignment depolarisation measurements, the monochromator was used with the minimum resolution possible ( $\approx 75 \text{ \AA}$ ), meaning the measurement was essentially unresolved. However, for the total disorientation measurements it was necessary to resolve emission from either the P or R branch to obtain a quantum beat, and for the elastic measurements to record just the fluorescence from the initially populated spin-rotation level. Therefore the monochromator was used at a higher resolution to disperse the fluorescence, up to  $1 \text{ \AA}$  for elastic measurements.

The experiments were performed in a uniform magnetic field of between 0 and 30 Gauss. The center of the reaction chamber was screened from external magnetic fields by  $\mu$ -metal shielding [3, 14–17, 21, 22]. For the alignment experiments, the axis of the magnetic field was aligned parallel to the fluorescence detection direction [3] while in the orientation experiments the field axis was directed perpendicular to the



detection axis, and to the pump laser propagation direction [15].

### 3.3. Zeeman beats

#### 3.3.1. Total depolarisation measurements

The non-zero nuclear magnetic moment of H and N splits the rotational levels of OH(A) and NO(A) into a number of hyperfine components, characterized by the total angular momentum  $\mathbf{F} = \mathbf{I} + \mathbf{j}$ . The applied magnetic field lifts the degeneracy of each of these hyperfine sublevels (Zeeman splitting) resulting in  $2F + 1$  components characterized by the quantum number  $M_F$  (the projection quantum number along the magnetic field direction).

The dye laser employed in the present work has a pulse duration of  $\sim 5$  ns, and hence quantum beats between levels split by more than  $\sim 30$  MHz will be unobservable. For OH(A), the hyperfine splitting is of the order of several hundred mega-Hertz [49, 50], hence only the beats between Zeeman components of the individual hyperfine sublevels are observed in the present work. However, the hyperfine level splittings for NO(A) are of the order of tens of megahertz so both hyperfine and Zeeman quantum beats could be observed. For the levels where it was chosen to observe Zeeman beats ( $N' \geq 5$ ), the hyperfine beats were of negligible intensity compared to the Zeeman and intermanifold beats.

For alignment measurements, the fluorescence decays in the Zeeman quantum beat experiments were fit using the following expression [51–54]:

$$I = A e^{-k_p t} \times \left[ 1 + e^{-k_d t} \sum_F C_F \cos(2\pi \alpha_F H t + \phi) \right] \quad (30)$$

In this equation,  $H$  is the magnetic field strength,  $\phi$  is the phase of the beat signal,

defined by the probe laser and detector polarisation geometries, and  $A$  and  $C_F$  are constants defining the total intensity and the relative beat amplitudes, respectively. The sum is over the two (OH(A)) or three (NO(A)) hyperfine levels corresponding to a single spin-rotation level. In the Hund's case (b) limit, appropriate to OH(A) and NO(A), the parameter  $\alpha_F$ , which defines the beat frequency per unit applied field, can be written to a good approximation as a function of the  $g_F$  factors of the excited state [51–54]

$$\alpha_F \simeq 2 \frac{\mu_0}{h} g_F \quad (31)$$

In the case of orientation measurements, the normalised difference between the signals obtained using left and right circularly polarised light ( $I_L$  and  $I_R$ , respectively) is fitted using the expression

$$C = \frac{I_L - I_R}{I_L + I_R} = e^{-k_d t} \sum_F C'_F \cos(2\pi\alpha'_F H t + \phi) \quad (32)$$

with  $\alpha'_F = \alpha_F/2$  [15].

Two phenomenological first order rate constants,  $k_p$  and  $k_d$ , have been introduced to allow for decay of the population and the angular momentum polarisation, respectively [55, 56]. These can be expressed as sums of rate constants describing collision-free and collision-induced decay processes:

$$\begin{aligned} k_p &= k_0 + k_1 [\text{Q}] \\ k_d &= k_2 + k_3 [\text{Q}] \end{aligned} \quad (33)$$

$k_2$  is associated with depolarisation in the absence of the quencher gas, which could arise, for example, from field inhomogeneities. Of particular interest to the current work is  $k_3$ , which accounts for the collisional depolarisation of the radical. This is

converted into a thermally averaged cross-section using the thermal mean relative velocity,  $\langle v_{\text{rel}} \rangle$ , via  $\sigma^{(k)} \simeq k_3 / \langle v_{\text{rel}} \rangle$ .

Typical thermal OH(A) Zeeman quantum beat decays obtained using left and right hand circularly polarised light are shown in the top row of figure 1 for He (left hand column), Ar (middle column) and Kr (right column). The quantum beats obtained by taking the difference between the signals as described above are shown, with fits, for 300 mTorr and 100 mTorr of quencher gas in the middle row and bottom row of the figure, respectively.

### 3.3.2. Elastic depolarisation measurements

For OH(A) the rotational energy level spacing is such that it is possible to record only the fluorescence from the initially populated spin-rotation level using a monochromator, allowing the rate of elastic depolarisation to be determined under thermal conditions experimentally. The elastic depolarisation cross sections can be obtained by fitting the spin-rotation state resolved data in the same way as the total data, *i.e.* using equation (32) for orientation and equation (30) for alignment. However, in the resolved case  $k_1$  is the sum of the electronic quenching and RET rate constants, and therefore RET and quenching cross sections can also be obtained from the elastic measurements.

### 3.4. Hyperfine beats

As mentioned above, for NO(A) the hyperfine splitting is sufficiently small for hyperfine levels of a given  $j$  to be excited coherently [16, 26]. The alignment induced by photon absorption then oscillates in time between  $\mathbf{j}$  and  $\mathbf{I}$  due to coupling with

the nuclear spin. The time dependence of the polarisation of both  $\mathbf{j}$  and  $\mathbf{I}$  have been discussed previously [57, 58], and in the former case is

$$A_0^{(2)}(j, t) = G^{(2)}(j, t) A_0^{(2)}(j, t = 0) \quad (34)$$

where

$$G^{(k)}(j, t) = \sum_{F, F'} \frac{(2F+1)(2F'+1)}{(2I+1)} \left\{ \begin{matrix} F' & F & k \\ j & j & I \end{matrix} \right\}^2 \cos[(E_F - E_{F'})t/\hbar] \quad (35)$$

where  $E_F$  represents the hyperfine energy levels of NO(A). Examples of hyperfine quantum beats obtained for  $N=2$  with a range of pressures of He (left column), Ar (middle column) and Kr (right column) are shown in figure 2. The black dashed line shows the experimental data, and the solid red line the fit to the data, obtained using the equation [16]:

$$I = A e^{-k_p t} \times \left[ 1 + e^{-k_d t} \sum_F C'_F \cos(2\pi\omega_F t + \phi) \right] \quad (36)$$

where  $\omega_F$  are the hyperfine splitting frequencies of NO(A). The latter were treated as adjustable parameters in the fits to the data, as were the beat amplitudes  $C'_F$ . In the present work, hyperfine quantum beats were used to obtain collisional disalignment data for NO(A) with a range of quencher gases in the initial state  $N=2$  and  $N=5$ .

### 3.5. Translational moderation of OH(A)

The OH(X) products from the 193 nm photodissociation of  $\text{H}_2\text{O}_2$  are born translationally excited, with a narrow velocity distribution centred near  $4950 \text{ m s}^{-1}$  for  $N'' = 4$  and  $4550 \text{ m s}^{-1}$  for  $N'' = 10$  [59]. The superthermal experiments described here were performed using a time-delay of 250 ns between the pump and probe lasers. On the timescales of the Zeeman beat experiments, translational moderation of both

the ground and excited states of OH can potentially compete with the collisional depolarisation process of interest.

Doppler-resolved LIF profiles, obtained over a range of delay-times, were compared with the results of a simple hard sphere model of the scattering dynamics, in which the angular distribution of the OH(X) products was assumed to be isotropic [3, 60]. The optimised model was used to provide estimates of the mean relative velocity appropriate to the pressure and time-delay conditions used in each of the Zeeman quantum beat experiments. The resulting velocities were  $2500\text{ m s}^{-1}$  for OH(A) + He,  $3900\text{ m s}^{-1}$  for OH(A) + Ar and  $3600\text{ m s}^{-1}$  for OH(A) + Kr. These relative velocities were then used to convert the experimentally measured rate coefficients into superthermal cross sections. Although these superthermal experiments are clearly not at a sharply defined collision energy, the simulations indicate that they do provide a simple approximate means of determining the qualitative effect of raising the collision energy on the depolarisation process.

### 3.6. Theoretical methods

#### 3.6.1. QM method

Fully quantum close-coupling (CC) scattering calculations of integral and tensor cross sections were performed on the *ab initio* OH( $A^2\Sigma$ )-Ar [13], OH( $A^2\Sigma$ )-Kr [22], NO( $A^2\Sigma$ )-He [28] and NO( $A^2\Sigma$ )-Ar [28] PESs using the HIBRIDON suite of codes [61], which employs a hybrid propagator comprised of the Log-Derivative propagator by Manolopoulos [62, 63] and the Airy propagator for the long-range region. Full details of all the parameters used in the calculations can be found in references

[13, 16, 21].

The HIBRIDON code calculates the scattering  $\mathbf{S}$  matrix, from which it is possible to obtain all observable properties of the system. The  $\hat{S}$  operator connects the initial and final total wavefunctions of the system at fixed total  $J$ :

$$\hat{S}|\Psi_{\text{in}}^J\rangle = |\Psi_{\text{out}}^J\rangle \quad (37)$$

The transition operator,  $\hat{T}$ , is then defined as  $\hat{1} - \hat{S}$ :

$$\begin{aligned} \hat{T}|\Psi_{\text{in}}^J\rangle &= (\hat{1} - \hat{S})|\Psi_{\text{in}}^J\rangle \\ &= |\Psi_{\text{in}}^J\rangle - |\Psi_{\text{out}}^J\rangle \end{aligned} \quad (38)$$

The elements of the  $\mathbf{T}$  matrix are used in the equations in section 2.2 to calculate the integral and tensor cross sections.

### 3.6.2. QCT method

Batches of approximately  $1 \times 10^5$  trajectories were run for several initial  $N$  states at fixed collision energies for the NO(A) + Rg and OH(A) + Rg systems. To obtain results to compare with the NO(A) + Rg and thermal OH(A) + Rg experimental measurements, a collision energy of 39 meV was used, which corresponds to the mean thermal energy at 300 K. It was found that calculations at this fixed collision energy were only slightly different to calculations run using a Maxwell-Boltzmann distribution of collision energies [22]. Superthermal OH(A) + Rg calculations were also run, using collision energies of 110 meV and 440 meV for OH(A) + He, 760 meV and 1.25 eV for OH(A) + Ar and 0.9 eV and 1.5 eV for OH(A) + Kr. These higher energies span the range estimated by considering the degree of moderation of OH(A) on the timescale of the present experiments (see Section 3.5).

The QCT method employed was similar to that described in reference [64], and will only be described briefly here. Since the PESs for OH(A) + Rg [13, 22] and NO(A) + Rg [28] have only been calculated using the fixed equilibrium bond lengths of the radicals, the method of Lagrange multipliers was used to force rigid rotor behavior during the integration of the classical equations of motion.

The impact parameter for the  $i$ -th trajectory was sampled according to  $b^{(i)} = \xi^{1/2} b_{\max}$ , where  $\xi$  is a random number in the  $(0, 1)$  interval. The maximum impact parameter leading to inelastic trajectories,  $b_{\max}$ , was determined by the criterion that no trajectories with  $\Delta N > 0.5$  took place for  $b > b_{\max}$ .

To assign the final state for each trajectory, the square of the final rotational angular momentum  $|\mathbf{N}'|^2 = N'(N' + 1)\hbar^2$  was first calculated, and then the values of  $N'$  thereby obtained were rounded to the nearest integer. Trajectories whose final  $N'$  state were found to lie between  $N \pm 0.5$  were considered elastic. The asymptotic angle between the initial  $\mathbf{N}$  and final  $\mathbf{N}'$  angular momentum vectors was obtained *via* the cosine rule [13]:

$$\cos \theta_{NN'} = \frac{\mathbf{N} \cdot \mathbf{N}'}{|\mathbf{N}||\mathbf{N}'|} \quad (39)$$

Using the final rotational states and  $\theta_{NN'}$  angles from the full set of trajectories, cross sections for RET and collisional depolarisation were calculated as described in section 2.4 and extended to the quasi open shell case using the method described in section 2.5.

### 3.6.3. TSH-QCT method

In contrast to the NO(A) + Rg, OH(A) + He and OH(A) + Ar systems, in which the scattering is almost entirely electronically adiabatic, the OH(A) + Kr system displays an appreciable degree of electronic quenching ( $\sigma_Q \simeq 8 \text{ \AA}^2$ ) [65]. To fully model the inelastic scattering in OH(A) + Kr, the quenching channel must be accounted for. This was done with the trajectory surface-hopping QCT (TSH-QCT) method [66], using the fewest switches algorithm described in reference [67].

The non-collinear approach of the Kr atom to the OH(X) ground state reduces the system's symmetry from  $C_{\infty v}$  to  $C_s$ , resulting in the doubly degenerate  $\Pi$  state splitting into two electronic states, labelled  $1A'$  and  $1A''$  according to their symmetry with respect to reflection in the scattering plane. The OH(A) electronic wavefunction is symmetric under such a reflection, so is labelled  $2A'$ . These three adiabatic potential energy surfaces have been calculated by Kłos *et al.* at the MRCISD+Q level of theory [30].

As states of different symmetry cannot couple electronically, the  $1A''$  state is the same in the adiabatic and diabatic representations. The diabatic states  $\Pi_{A'}$  and  $\Sigma_{A'}$  are related to the adiabatic states by an orthogonal transformation [26, 30]:

$$\begin{pmatrix} V_{1A'} & 0 \\ 0 & V_{2A'} \end{pmatrix} = \mathbf{C} \begin{pmatrix} V_{\Pi_{A'}} & V_{\Sigma_{\Pi}} \\ V_{\Sigma_{\Pi}} & V_{\Sigma_{A'}} \end{pmatrix} \mathbf{C}^T \quad (40)$$

in which

$$\mathbf{C} = \begin{pmatrix} \cos \alpha & \sin \alpha \\ -\sin \alpha & \cos \alpha \end{pmatrix} \quad (41)$$

In the two state TSH-QCT model, trajectories were propagated on the adiabatic



$2A'$  and  $1A'$  PESs as in reference [26], and the kinetic coupling between them was evaluated from the product of the nuclear velocities with the non-adiabatic coupling matrix elements (NACMEs). The NACMEs are given by the derivative of the mixing angle,  $\alpha$  in equation (41), which can be calculated from the adiabatic potentials  $1A'$ ,  $1A''$  and the diabatic electronic coupling  $V_{\Sigma\Pi}$  [30].

Although coupling between states of  $A'$  and  $A''$  symmetry is forbidden, it is possible for a rotation of  $A''$  symmetry to couple to the electronic degrees of freedom, resulting in a transition that is allowed overall. These roto-electronic (Coriolis or Renner-Teller) transitions mean that the  $1A''$  state must also be included in the TSH-QCT theory for an accurate picture of the non-adiabatic dynamics. A three state TSH-QCT model was set out in reference [27], in which three mixing angles are used to describe the couplings between the potentials. Extra terms were taken from the rotational Hamiltonian in order to describe the roto-electronic couplings and calculate the other two mixing angles ( $\beta$  and  $\omega$ ), as described in reference [27].

As for the single-state QCT calculations, it was found that the fixed collision energy results were almost the same as those obtained from a Maxwell-Boltzmann distribution of collision energies [27].

## 4. Depolarisation in triatomic systems

### 4.1. QM vs QCT calculations for $\text{OH}(A) + \text{Rg}$ and $\text{NO}(A) + \text{Rg}$

From here on, all calculations reported in this review (QM and QCT) use a fixed collision energy. For comparison with thermal experimental data (300 K), this energy is taken as 0.039 eV, corresponding to the mean thermal collision energy at 300 K.

As explained in sections 3.6.2 and 3.6.3, the fixed energy calculations provide a very good approximation to those performed using a Maxwell-Boltzmann distribution of energies.

A comparison of the results from the fixed energy *closed shell* QM (open squares) and QCT (filled squares) calculations is presented in figure 3, for  $N=2$  resolved into final rotational state  $N'$ . Cross-sections for RET, total (elastic + inelastic) disorientation and total disalignment are compared for NO(A) + Ar at 0.039 eV, OH(A) + Ar at 0.4 eV ('superthermal') and OH(A) + Ar at 0.039 eV. The two sets of calculations are generally in good agreement, demonstrating that the use of QCT is appropriate for these systems. The QCT calculations are, however, unable to account for the parity dependent alternation in the magnitude of the NO(A) + Ar cross sections with  $N'$ , which arises due to the near homonuclear character of the NO molecule, seen in fully state resolved QM calculations.

On increasing the collision energy for OH(A) + Ar from 0.039 eV to 0.4 eV, it can be seen that significantly more  $N'$  levels are populated by collisions, as would be expected as more rotational levels become energetically accessible. This also results in a decrease in the depolarisation cross sections, the reasons for which will be discussed later in the section.

Quasi-*open shell* QCT (filled triangles) results (section 2.5) are compared with those obtained from QM calculations (open triangles) in figure 4, for  $N=2$ ,  $j=1.5$ . Note that these results are fully resolved in both initial and final rotational state. The downward pointing triangles show the cross sections for collisions that conserve the initial spin-rotation state ( $N - 1/2 \rightarrow N' - 1/2$ ) and the upward pointing triangles

those which change the spin-rotation state ( $N - 1/2 \rightarrow N' + 1/2$ ). Again, the top row shows the RET cross sections, the middle row the disorientation cross sections and the bottom row the disalignment cross sections.

The agreement between the open shell QM and QCT calculations is very good for OH(A) + Ar at 0.4 eV (middle column) and for OH(A) + Kr under thermal (0.039 eV) conditions (right column), but less so for (thermal) NO(A) + He shown in the left hand column. This is particularly the case when  $\Delta N = \pm 1$ , where the QCT cross sections are significantly larger than their QM counterparts. The reason for this is the binning procedure used in the QCT calculations, where any trajectories where  $|\Delta N| > 0.5$  are treated as inelastic. Gaussian binning has also been applied [68, 69], but the results were very similar to those presented here using histogram binning. It should be noted that using the constraint  $|\Delta N| \geq 1$  to define an inelastic trajectory brings the QCT and QM results into much better agreement. Equivalently, restricting  $\Delta K > 1$  as opposed to  $\Delta K > 0.5$  for the depolarisation cross sections results in much better agreement between the QCT and QM calculations.

#### 4.2. Rotational energy transfer for OH(A) + Rg and NO(A) + Rg

Fluorescence decays derived from the sum of those recorded using left and right circularly polarised light (or orthogonal linearly polarised light) when making the OH(A) + Rg elastic depolarisation measurements were fitted to obtain the total RET cross sections, summed over final  $j'$  states for  $j' \neq j$ . The results obtained are shown in figure 5, where the experimental results (filled triangles) are compared with the results from fixed energy QCT calculations (open squares) for different initial

rotational states. The top row is for the initial  $f_2$  ( $N - S$ ) spin-rotation levels, and the bottom row the initial  $f_1$  ( $N + S$ ) spin-rotation levels, for OH(A) + He (left column), OH(A) + Ar (middle column) and OH(A) + Kr (right column).

In all cases, the total RET cross sections drop with increasing  $N$ , as expected as a greater energy needs to be transferred at higher  $N$  for an inelastic collision to take place. The agreement between the experimental and QCT cross sections is excellent for OH(A) + Ar and OH(A) + Kr, but in the case of OH(A) + He the QCT cross sections significantly overestimate those observed experimentally. However, the experimental results are in better agreement with the results from QM calculations obtained by Jörg *et al.* [70] using their PES, shown in the left panels of the figure as open circles. As shown in figure 3, the QCT calculations overestimate the RET cross sections for NO(A) + He, and this could also be the case for OH(A) + He. Again, restricting inelastic trajectories to those where  $|\Delta N| \geq 1$  results in the QCT calculations improves the agreement with the previous QM calculations. The RET cross sections obtained experimentally are also in good agreement with those obtained in earlier experiments by Jörg *et al.* [71], shown as filled circles in the bottom left hand panel.

There have also been previous experimental studies of RET in OH(A) + Ar [71, 72]. Unlike in the present work, these were resolved into final spin-rotation level. However, summing these results over final rotational level,  $j'$ , allows comparisons to be made with the data shown here. The results from Jörg *et al.* [71] for the  $f_2$  spin-rotation level are shown as filled circles in the top panel, and the results from Lengel and Crosley [72] for the  $f_1$  spin-rotation level are shown as filled circles in the bottom

panel. The agreement between the current and previous data is excellent for the  $f_2$  spin-rotation level, but the previous results are significantly smaller than those obtained here both experimentally and theoretically for the  $f_1$  spin-rotation level. To obtain the RET cross sections, only the first 100 ns of the data was fit to avoid possible complications that could arise from significant back-transfer of population back to the initially prepared spin-rotation state. It is possible that this could account for some of the discrepancy between the previous study and the results presented here, although this is likely to be more significant at lower  $N$ .

Results from an earlier QM study of RET in  $\text{OH(A)} + \text{Ar}$  performed by Esposti and Werner [73] are shown as open circles in the middle column of figure 5. There is again excellent agreement between the current experimental data, and results from the QCT calculations, again validating the use of the QCT method.

Although it is possible to measure the total RET cross sections for  $\text{OH(A)} + \text{Rg}$  experimentally, the resolution of the experiment is not sufficient to allow these to be measured for  $\text{NO(A)} + \text{Rg}$ . However, they can be found theoretically. Figure 6 shows QCT total RET cross sections for  $\text{NO(A)}$  with He, Ar and Kr, compared with experimental results obtained in references [74] for He and [75] for Ar. As in the case of  $\text{OH(A)} + \text{Rg}$ , the QCT calculations do a good job of modelling RET in these systems. The RET cross sections again drop with  $N$ , due to larger energy gaps between higher rotational levels, and more RET is observed as the PESs become more attractive.

Figure 7 presents a comparison of the RET cross sections obtained from QCT calculations run at a fixed collision energy of 0.039 eV for  $\text{OH(A)}$  (top row) and

NO(A) (bottom row), in collisions with He (left column), Ar (middle column) and Kr (right column). The total RET cross sections are resolved into transitions which change only the spin-rotation level,  $j$ , but conserve  $N$  (the white section of the bar), transitions which change both the rotational level,  $N$ , and  $j$  (the striped section of the bar) and those which change  $N$  but conserve  $j$  (the filled section of the bar). All the cross sections presented are for the  $f_2$  spin-rotation level. The total height of the bar shows the total RET cross-section, and as can be seen these are larger for NO(A) + Rg than OH(A) + Rg. This is due to the different moments of inertia associated with each of the radicals, which results in a smaller rotational energy level spacing for NO(A) + Rg than OH(A) + Rg. Therefore, RET is more favoured in NO(A) with respect to OH(A).

It can also be seen that collisions which change only the spin-rotation state are more significant in OH(A) than in NO(A). In the limit that electron-spin is a spectator, spin-rotation changing collisions are brought about by a change in the direction of  $\mathbf{N}$ . The NO(A) + Rg PESs are less anisotropic than the OH(A) + Rg PESs, and therefore less efficient at bringing about spin-rotation changing collisions. This point is particularly apparent at higher  $N$ , where the main contribution to the OH(A) + Rg RET cross sections is from spin-rotation changing but  $N$  conserving transitions, whilst for NO(A) + Rg the main contribution is from spin-rotation conserving (but  $N$  changing) collisions. Again this can be attributed to the smaller rotational spacing between the energy levels in NO(A) than OH(A), which means collisions which change  $N$  occur more readily in NO(A) than OH(A).

### 4.3. Total (elastic + inelastic) depolarisation

#### 4.3.1. $\text{NO(A)} + \text{Rg}$ , 300 K

The total (thermal) disorientation (top row) and disalignment (bottom row) cross sections are shown for  $\text{NO(A)} + \text{He}$  (left column),  $\text{NO(A)} + \text{Ar}$  (middle column) and  $\text{NO(A)} + \text{Kr}$  (right column) in figure 8. All the results presented are for the  $f_2$  spin-rotation level and are summed over final rotational state ( $j' \neq j$ ). As can be seen, the experimental results (filled triangles) fall as the initial rotational level,  $N$ , increases. This reflects the larger momentum transfer required to change the direction of a larger  $\mathbf{N}$  compared to a smaller  $\mathbf{N}$  by the same angle, which will occur at smaller impact parameters,  $b$ . It should also be noted that the disorientation cross sections tend to be smaller than the disalignment cross sections, as it is harder to change the sense of rotation of the radical than the axis of rotation.

The results from the QCT calculations are also shown in the figure as open squares. There is good agreement between the experimental and theoretical values of the cross sections. The depolarisation cross sections are large, implying that depolarisation occurs *via* a long range interaction. However, the  $\text{NO(A)} + \text{He}$  cross sections are significantly smaller than those observed for  $\text{NO(A)} + \text{Ar}$  and  $\text{NO(A)} + \text{Kr}$ . This could either be due to kinematic effects (the light mass of the He means that its associated momentum is small) or the potential energy surface, which in the case of  $\text{NO(A)} + \text{He}$  has a well depth of  $<1 \text{ cm}^{-1}$  [28] and so is almost purely repulsive. To separate these effects, QCT calculations were performed for  $N=7$  using the  $\text{NO(A)} + \text{He}$  masses on the  $\text{NO(A)} + \text{Kr}$  PES (denoted  $\text{NO-}^4\text{Kr}$ ) and the  $\text{NO(A)} + \text{Kr}$  masses

on the  $\text{NO(A)} + \text{He}$  PES (denoted  $\text{NO-}^{83.8}\text{He}$ ). The results from these calculations are presented in figure 9, along with the results from calculations using the correct mass and PES combinations (denoted as  $\text{NO-}^4\text{He}$  and  $\text{NO-}^{83.8}\text{Kr}$ ). The left hand panel of the figure shows that changing the mass (*e.g.*, from  $\text{NO-}^4\text{Kr}$  to  $\text{NO-}^{83.8}\text{Kr}$ ) does not significantly change the state-to-state RET cross sections, but that changing from the  $\text{NO(A)} + \text{He}$  to the  $\text{NO(A)} + \text{Kr}$  PES (*e.g.*, going from  $\text{NO-}^4\text{He}$  to  $\text{NO-}^4\text{Kr}$ ) results in an increase in the RET cross sections. This reflects the longer range of the  $\text{NO(A)} + \text{Kr}$  PES compared to that for  $\text{NO(A)} + \text{He}$ .

The state-to-state disorientation and disalignment cross sections are shown in the middle and right panel of figure 9, respectively. Again the depolarisation cross sections increase on changing from the  $\text{NO(A)} + \text{He}$  to  $\text{NO(A)} + \text{Kr}$  PES. This will be partly due to the increase in RET cross sections already discussed, but also the increased anisotropy of the  $\text{NO(A)} + \text{Kr}$  PES, which has a well depth of  $\approx 140 \text{ cm}^{-1}$  [28]. However, unlike in the case of the RET cross sections, the kinematics also influence the depolarisation cross sections. On going from the He mass to the Kr mass, the depolarisation cross sections increase. This increase is most significant in the case of the elastic depolarisation cross-section, with the Kr mass causing more elastic depolarisation on both PESs than the He mass. Therefore, the small size of depolarisation cross sections observed for  $\text{NO(A)} + \text{He}$  is due to both the small mass of the He and the impulsive nature of the PES.



4.3.2.  $\text{OH}(\text{A}) + \text{Rg}$ , 300 K

Unlike the  $\text{NO}(\text{A}) + \text{Rg}$  depolarisation cross sections, which were only recorded for the  $f_2$  spin-rotation level, the total depolarisation cross sections for  $\text{OH}(\text{A}) + \text{Rg}$  were measured for either the  $f_1$  or  $f_2$  spin-rotation level for a range of initial  $N$ . Figure 10 presents the total thermal disorientation (top row) and disalignment (bottom row) cross sections for the  $f_1$  and  $f_2$  spin-rotation levels, obtained from QCT calculations for  $\text{OH}(\text{A}) + \text{He}$  (left column),  $\text{OH}(\text{A}) + \text{Ar}$  (middle column) and  $\text{OH}(\text{A}) + \text{Kr}$  (right column). It should be noted that there is no  $f_2$  spin-rotation level for  $N=0$ , and that it is not possible to align at state with  $j=0.5$ . In all cases, the depolarisation cross sections are larger for the  $f_2$  spin-rotation level than for the  $f_1$  spin-rotation level, with the difference more pronounced at lower  $N$ . As mentioned previously, the electron spin can be treated as a spectator to the collision. From simple geometric arguments it follows that a given change in the direction of  $\mathbf{N}$  causes more depolarisation for  $f_2$  than for  $f_1$ , where this difference is more significant at low  $N$ .

The total thermal depolarisation cross sections for  $\text{OH}(\text{A}) + \text{He}$  (left column),  $\text{OH}(\text{A}) + \text{Ar}$  (middle column) and  $\text{OH}(\text{A}) + \text{Kr}$  (right column) are presented in figure 11. The top row shows the disorientation cross sections and the bottom row the disalignment cross sections. The experimental results are shown as filled triangles, with those pointing upwards showing the cross sections for the  $f_1$  spin-rotation level, and those pointing downwards the  $f_2$  spin-rotation level. For  $\text{OH}(\text{A}) + \text{He}$  and  $\text{OH}(\text{A}) + \text{Ar}$ , the depolarisation cross sections follow the same trends already discussed for the  $\text{NO}(\text{A}) + \text{Rg}$  cross sections, which will not be repeated here. However, the trend observed experimentally for  $\text{OH}(\text{A}) + \text{Kr}$  is significantly different, with the cross

sections increasing to  $N=8$  before falling slightly to  $N=14$ .

The adiabatic QCT results are also included in the figure as open squares. These are in excellent agreement with the experimental values for  $\text{OH(A)} + \text{He}$  and  $\text{OH(A)} + \text{Ar}$  but they fail to capture the unusual trend observed in the  $\text{OH(A)} + \text{Kr}$  depolarisation cross sections. This is not a failure of the QCT method; as shown in figure 4, the QM and QCT results are in excellent agreement for  $\text{OH(A)} + \text{Kr}$ .

A possible explanation for this discrepancy is that electronic quenching is significant in  $\text{OH(A)} + \text{Kr}$  [26, 30, 65], in contrast to  $\text{OH(A)} + \text{He}$ ,  $\text{OH(A)} + \text{Ar}$  and the  $\text{NO(A)} + \text{Rg}$  systems considered here, where it can safely be neglected. This quenching is obviously not included in the single-surface QCT calculations. From the comparison between experimental and adiabatic (single PES) calculations, it is apparent that electronic quenching is more important for lower  $N$  states [26, 30, 65]. Section 4.6 investigates further the effects of electronic quenching on the cross sections for collisional depolarisation in  $\text{OH(A)} + \text{Kr}$ .

#### 4.3.3. $\text{NO(A)} + \text{Rg}$ vs $\text{OH(A)} + \text{Rg}$ , 300 K

To determine whether the differences in the state-to-state RET and depolarisation cross sections for the  $\text{OH(A)} + \text{Rg}$  and  $\text{NO(A)} + \text{Rg}$  systems are due to kinematic effects or differences in the PESs, closed shell QCT calculations were run for  $N=5$  using the  $\text{NO(A)} + \text{Ar}$  masses on the  $\text{OH(A)} + \text{Ar}$  PES (denoted  $\text{O}^{14}\text{H-Ar}$ ) and the  $\text{OH(A)} + \text{Ar}$  masses on the  $\text{NO(A)} + \text{Ar}$  PES (denoted  $^{14}\text{NO-Ar}$ ). The results from these calculations are presented in figure 12, along with the results from calculations using the correct mass and PES combinations (denoted as  $^{14}\text{NO-Ar}$  and  $\text{O}^{14}\text{H-Ar}$ ).

Changing from the OH mass to the NO mass (*e.g.*, on going from  $^1\text{NO-Ar}$  to  $^{14}\text{NO-Ar}$ ) increases the state-to-state RET cross sections, shown in the left hand panel of the figure, and increases the number of final rotational states populated by the collision. This is due to the different moments of inertia associated with each of the mass combinations, which results in a smaller energy spacing between rotational levels for  $^{14}\text{NO-Ar}$  than  $^1\text{NO-Ar}$ . For the same reason, elastic depolarisation is more important for  $^1\text{NO-Ar}$  than  $^{14}\text{NO-Ar}$ , as shown in the middle panel for disorientation and the right panel for disalignment. Changing the PES also has an effect on the RET and depolarisation cross sections. On going from  $^{14}\text{NO-Ar}$  to  $\text{O}^{14}\text{H-Ar}$  the depolarisation cross sections drop slightly. This is due to a decrease in the RET cross sections, because the  $\text{OH(A)} + \text{Ar}$  PES is shorter range than the  $\text{NO(A)} + \text{Ar}$  PES. However, on changing the PES for the OH mass combination, *i.e.* going from  $^1\text{NO-Ar}$  to  $\text{O}^1\text{H-Ar}$  results in an increase in the RET cross sections. The  $\text{NO(A)} + \text{Ar}$  PES is too isotropic to bring about significant RET when the energy spacing of the radical is larger. Therefore, both the RET and depolarisation cross sections are influenced by kinematics and the differences in the anisotropy and range of the PESs.

#### 4.3.4. Superthermal $\text{OH(A)} + \text{Rg}$

It is possible to increase the collision energy of the  $\text{OH(A)} + \text{Rg}$  systems by decreasing the time delay between the pump and the probe lasers. These ‘superthermal’ collision energy total depolarisation results are shown in figure 13. The top row shows the total disorientation cross sections and the bottom row the total disalignment cross sections for  $\text{OH(A)} + \text{He}$  (left column),  $\text{OH(A)} + \text{Ar}$  (middle column) and  $\text{OH(A)} +$

Kr (right column), for initial  $f_1$  and  $f_2$  spin-rotation levels. The mean velocities used to convert the rate constants to cross sections are those reported in section 3.5.

In all cases, the total depolarisation cross sections tend to decrease with increasing  $N$ , as observed in the NO(A) + Rg systems. The cross sections are also smaller than the thermal cross sections presented in figure 11. As shown in figure 3, as the collision energy is increased, the RET cross section increases as there is sufficient energy available to populate more rotational states. The depolarisation cross sections are related to the RET cross sections *via*  $\sigma^{(k)} = \sigma^{(0)}(1 - a^{(k)})$  (section 2.4). It follows that the collisions must become less depolarising ( $a^{(k)}$  closer to 1) as the collision energy is increased.

The results from the QCT calculations are also shown for the same spin-rotation level as recorded experimentally in figure 13 at two fixed collision energies. The QCT results capture the trends in the depolarisation cross sections, even if they tend to overestimate the values of the cross sections observed experimentally. A possible reason for the disagreement between the experimental and theoretical cross sections is that the QCT calculations are run at a fixed, well defined collision energy, whereas the experiment samples a range of collision energies. As shown in the figure, the depolarisation cross sections are almost independent of collision energy in the range that is sampled experimentally. Given the uncertainties in the extent to which translational moderation occurs experimentally, the agreement between the QCT calculations and the experimental results is considered to be reasonable.

In the case of OH(A) + Kr, the agreement between experiment and theory is much better than that observed in the thermal (300 K) case. The quenching cross-section

is expected to decrease with collision energy and, indeed, this is the case. For the  $f_1$  level of  $N = 5$ , the measured quenching cross sections are  $3.2 \pm 1.2 \text{ \AA}^2$  at 300 K [30] and  $1.19 \pm 0.15 \text{ \AA}^2$  at 1900 K [76], demonstrating a fall with temperature that is also seen for other colliders [77]. The increased agreement of depolarisation cross sections with QCT at higher temperatures further supports the idea that electronic quenching is responsible for the discrepancies.

#### 4.4. Elastic depolarisation of OH(A) + Rg, 300 K

The thermal (300 K) elastic disorientation (top row) and disalignment (bottom row) cross sections are presented in figure 14 for OH(A) + He (left column), OH(A) + Ar (middle column) and OH(A) + Kr (right column). It should be noted that the  $N=0, j=0.5$  disorientation cross-section is necessarily zero. The only contribution to the angular momentum is the electron (and nuclear) spin, which act as spectators to the collision. Therefore their direction cannot be changed by the collision, and no depolarisation can occur.

In general, there is good agreement between the theoretical (open squares) and experimental (filled triangles) results. The exception to this is the disalignment cross sections for OH(A) + Ar, where the QCT calculations significantly underestimate the cross sections observed experimentally. The low  $N$  alignment data were measured using Q branch emission, and therefore the recorded signal included emission from an unresolved satellite line. This has the effect of making the experiment additionally sensitive to collisions which conserve  $N$ , but change spin-rotation level. As shown in the top panels of figure 7, these spin-rotation level changing collisions (represented

by the white section of the bar) have large cross sections. These collisions also result in significant dephasing, as the  $g_F$  values have opposite signs for the  $f_1$  and  $f_2$  spin-rotation levels. To account for this effect, detailed simulations were run for OH(A) + Ar and OH(A) + Kr, the results of which are shown as open circles in the bottom panels of figure 14. As can be seen, this leads to excellent agreement between the theoretical values of the disalignment cross sections for OH(A) + Ar, but results in the theoretical calculations overestimating the observed cross sections in OH(A) + Kr. It should be noted that the  $N=8$  and  $N=14$  alignment data and all the orientation data was recorded using either the P or R branch, and therefore satellite lines did not contribute to the signal.

Brinkman and Crosley [78] have measured elastic disalignment cross sections for OH(A) + He and OH(A) + Ar, and their results are shown as black triangles in the bottom panels of the figure. In both cases, the results are smaller than observed in the current study. However, as mentioned above, this is likely to be due to the unresolved satellite lines increasing the values obtained here. The elastic cross sections obtained by Brinkman and Crosley are in excellent agreement with the values obtained from the QCT calculations.

The trends observed in the OH(A) + He, OH(A) + Ar and OH(A) + Kr elastic depolarisation cross sections are strikingly different. As has been discussed previously [17], efficient elastic depolarisation is brought about by ‘following’ type trajectories, where the Rg atom is trapped in a complex with the radical due to the anisotropy of the PES. As the OH(A) + He PES has a well depth of  $\approx 120 \text{ cm}^{-1}$ , and the He will be travelling too quickly to sample the shallow potential well, complexes do not form.

The elastic cross sections therefore fall with increasing  $N$ , as would be expected for impulsive collisions. Both the OH(A) + Ar (well depth  $\approx 1700\text{ cm}^{-1}$  [5]) and OH(A) + Kr (well depth  $\approx 6000\text{ cm}^{-1}$  [22]) PESs are anisotropic enough for complexes to form at low  $N$ , leading to efficient elastic depolarisation. As  $N$  increases, the rotation of the radical ‘washes out’ the anisotropy of the PES, meaning the approaching Rg samples a rotationally averaged potential. However, the elastic cross sections remain large at high  $N$  for both OH(A) + Ar and OH(A) + Kr, suggesting this rotational averaging is not sufficient to suppress elastic depolarisation.

Costen *et al.* have used two colour polarisation spectroscopy to measure the collisional depolarisation of OH(A) + He and OH(A) + Ar [17]. The results obtained from these experiments,  $\sigma_{\text{ps}}$ , correspond to the sum of the RET and elastic depolarisation cross sections. Figure 15 presents a comparison of these cross sections obtained by Costen *et al.* for OH(A) + He (left column) and OH(A) + Ar (right column) with the sum of the RET and elastic depolarisation cross sections obtained here. The top panels correspond to loss of orientation and the bottom panels loss of alignment. It should be noted that the OH(A) + Ar elastic disalignment data has been corrected using the QCT results to account for the presence of the unresolved satellite line. This correction is not applied to the OH(A) + He data, where the cross sections for pure spin-rotation changing collisions are smaller. As shown in the figure, there is excellent agreement between the two sets of experimental data. The results from the Zeeman quantum beat experiments are for  $v=0$ , and those from the two colour polarisation spectroscopy experiments are for  $v=1$ . The good agreement between the two sets of results suggests that RET and depolarisation are not sensitive to the initial

vibrational state of OH(A).

The contribution that elastic depolarisation makes to the total depolarisation cross sections is shown in figure 16. The top six panels show the total thermal depolarisation cross sections (filled triangles) and elastic thermal depolarisation cross sections (open triangles) obtained experimentally for OH(A), for both disorientation and alignment. The bottom six panels present the total (thermal) depolarisation cross sections obtained experimentally for NO(A) + Rg, and the elastic depolarisation cross sections obtained from QCT calculations (open squares). The left hand column shows the results for He, the middle column Ar and the right hand column Kr. In the NO(A) + Rg systems, the elastic depolarisation cross sections make a far less significant contribution to the total depolarisation cross sections than in the case of collisions of OH(A) with Rg. This again reflects the smaller rotational energy level spacing in NO(A) than OH(A) due to their different moments of inertia, which makes inelastic collisions more probable in NO(A) than OH(A). In both OH(A) and NO(A), the contribution that elastic depolarisation makes to the total depolarisation cross sections increases as  $N$  increases. As shown in figures 5 and 7, the RET cross sections drop as  $N$  increases as more energy transfer is required. Therefore elastic collisions become relatively more important at higher  $N$ .

#### 4.5. Inelastic depolarisation of OH(A) + Rg, 300 K

Because both the total depolarisation cross sections and the elastic depolarisation cross sections have been determined for OH(A) + Rg, it is possible to find the inelastic depolarisation cross sections by subtraction. The total RET and inelastic de-



polarisation cross sections, summed over all  $j' \neq j$ , are related as in section 2.4. Therefore, comparing the total inelastic (RET) cross-section with the total inelastic depolarisation cross-section provides a direct measure of the polarisation parameters  $a^{(k)}$ .

For OH(A) under thermal conditions, the inelastic depolarisation cross sections were calculated using experimental data as far as possible, but using results from the QCT calculations where no experimental results were available. For comparisons to thermal NO(A) and OH(A) under superthermal conditions, the inelastic depolarisation cross sections were obtained using the total depolarisation cross sections obtained experimentally, and the elastic cross sections from the QCT calculations. In these two cases, the RET cross sections were also taken from the QCT calculations, although the RET cross sections for thermal OH(A) + Rg are also available from experimental results.

The inelastic disorientation and disalignment cross sections are compared with the total RET cross sections in figure 17. The top row of the figure corresponds to thermal OH(A), the middle row to superthermal OH(A), and the bottom row NO(A), in collisions with He (left column), Ar (middle column) and Kr (right column).

For NO(A) + He, the inelastic depolarisation cross sections are significantly smaller than the RET cross sections. The collisions do not cause much depolarisation and  $a^{(k)}$  is close to 1. As the mass of the Rg is increased, the collisions become more depolarising, although at higher  $N$  the RET cross sections still tend to be larger than the inelastic depolarisation cross sections, even for NO(A) + Kr. Therefore, for NO(A) + Rg depolarisation is relatively inefficient compared to RET.

In contrast to the  $\text{NO(A)} + \text{Rg}$  systems, the inelastic depolarisation cross sections for  $\text{OH(A)} + \text{Rg}$  are of a similar magnitude to the RET cross sections. This is the case even for  $\text{OH(A)} + \text{He}$ , the PES for which has a well depth of  $\approx 120 \text{ cm}^{-1}$  which is comparable to that for  $\text{NO(A)} + \text{Kr}$  ( $140 \text{ cm}^{-1}$ ). This corresponds to the collisions randomising the direction of  $\mathbf{j}$ , and  $a^{(k)} \approx 0$ . The inelastic disalignment cross sections in  $\text{OH(A)} + \text{Kr}$  tend to be larger than the RET cross sections. Therefore, the rate of depolarisation is faster than the rate of collisions, and  $a^{(2)}$  is negative. As the collision energy is increased, the magnitude of the inelastic depolarisation cross sections decreases compared to the RET cross sections. In all cases, the RET cross sections are larger than the inelastic depolarisation cross sections, so  $a^{(k)} > 0$ . Therefore the behaviour of the  $\text{OH(A)} + \text{Rg}$  systems at a higher collision energy starts to resemble that observed in  $\text{NO(A)} + \text{Rg}$ .

#### 4.6. Non-adiabatic effects in $\text{OH(A)} + \text{Kr}$

As remarked upon in section 4.3.2, there is some disagreement between experimental and QCT cross sections for collisional depolarisation in  $\text{OH(A)} + \text{Kr}$ , particularly for the  $f_2$  spin-rotation levels. This stands in contrast to  $\text{NO(A)} + \text{Rg}$  and lighter  $\text{OH(A)} + \text{Rg}$  systems, where experiment and QCT display excellent agreement. One plausible reason for this discrepancy is electronic quenching, which is competitive with RET in the  $\text{OH(A)} + \text{Kr}$  system [26, 30] but negligible in other systems considered here. Quenching takes place *via* a conical intersection near the bottom of the deep HO–Kr well [30], which is also the region of the PES most responsible for RET and inelastic depolarisation due to its strong attractive interactions and anisotropy [26]. This im-

plies that quenching and inelastic depolarisation are in direct competition, so many adiabatic trajectories that contribute most to the calculated RET and depolarisation cross sections should in fact be lost to quenching. Elastic depolarising collisions, on the other hand, occur at longer range than those leading to RET, inelastic depolarisation or quenching, thus explaining why agreement with adiabatic QCT is better in this case. A more in-depth discussion of these points is deferred to section 5.4, in which opacity functions are compared for the various collisional processes at work.

Quenching cross sections,  $\sigma_Q$ , for thermal (300 K)  $\text{OH(A)} + \text{Kr}$  are displayed in figure 18. It can be seen that the experimental results [30] are in good agreement with the previous results of Hemming *et al.* [65]. The rapid decrease in  $\sigma_Q$  with  $N$  explains why agreement of experimental and adiabatic QCT depolarisation is better at higher  $N$ .

In order to account for the effects of quenching on RET and collisional depolarisation, fixed-energy (0.039 eV) TSH-QCT calculations were performed using both the two state and three state models described in section 3.6.3 and in references [26, 27, 30], and quenching cross sections from these two models are compared to experiment in the left and right hand panels of figure 18, respectively. Including only quenching to the  $1A'$  PES *via* the conical intersection succeeds in capturing the trend of quenching with  $N$ , but is seen to underestimate its true magnitude by up to half. To fully model quenching in this system, it is necessary to include rovibronic couplings to the  $1A''$  state, resulting in the excellent agreement with experiment seen in the three-state model in the right hand panel of figure 18.

Calculated TSH-QCT cross sections for total RET and depolarisation from the

three state model are compared to adiabatic QCT and experiment in figure 19. Including quenching in the theory results in an improved agreement with experimental RET, as the calculated cross sections fall relative to the adiabatic results. However, due to the magnitude of quenching in this system, both the adiabatic and non-adiabatic theories can satisfactorily account for the observed RET within experimental error. Current work on the OH(A)-Xe system, in which the quenching cross sections are much larger [65], should demonstrate these effects more clearly.

As expected, the TSH-QCT calculations lower the cross sections for collisional depolarisation relative to adiabatic QCT, however the change is not enough to bring the results into agreement with experiment. This is particularly true for the  $f_2$  spin-rotation level; agreement for  $f_1$  is much better. A full quantum mechanical treatment of the system, including all states and couplings, would be desirable in order to see how good an approximation the present semiclassical method is; in addition, ongoing work on the OH(A)-Xe system aims to investigate these effects in a system where quenching is more extensive.

#### **4.7. Comparison to CN(A) + Ar**

Costen and co-workers have recently studied elastic depolarisation and RET in CN(A<sup>2</sup>Π,  $v = 4$ ) + Ar, in references [18, 25] and reviewed in reference [24]. The differential cross sections for selected inelastic transitions in CN(A) + Ar have also been recently measured [79]. This collision system has the same kinematics as the NO(A) + Ar system considered in this work, but, as a Π state, is more naturally compared to collisions of OH(X) and NO(X). Rate constants were measured for RET and

elastic depolarisation, and compared to adiabatic quantum scattering calculations on a new PES [25].

Collisions in this system occur on two PESs,  $V_{\text{sum}}$  and  $V_{\text{dif}}$  [80], of which  $V_{\text{sum}}$  is mostly responsible for elastic depolarising behaviour [24]. The  $V_{\text{sum}}$  PES in reference [25] has a well of  $D_0 = 110 \text{ cm}^{-1}$  in the T-shaped geometry, which is somewhat deeper than previous theoretical determinations [81] and comparable to the well depths in the  $\text{OH(A)} + \text{He}$  or  $\text{NO(A)} + \text{Ar}$  potentials.

The results of Costen and co-workers [25] for total RET and elastic depolarisation (disorientation and disalignment) are presented in figure 20. RET in the  $\text{CN(A)} + \text{Ar}$  system is much faster than elastic depolarisation, which is seen to be a relatively minor process [25] – inelastic depolarisation dominates over elastic. Comparing  $\text{CN(A)} + \text{Ar}$  to the  $\text{OH(A)} + \text{He}$  and  $\text{NO(A)} + \text{Ar}$  systems, this behaviour is much more like that seen with NO, due to both CN and NO being near-homonuclear diatomics with similar moments of inertia. A smaller rotational spacing than that of OH leads to more RET and inelastic depolarisation over elastic depolarisation. This trend is reinforced by the weak attractive forces seen in both  $\text{CN(A)} + \text{Ar}$  and  $\text{NO(A)} + \text{Ar}$  in contrast to, for example,  $\text{OH(A)} + \text{Ar}$ , in which elastic depolarisation is a much more important process.

Reference [25] (figure 20) shows a comparison of the experimental rate constants to those obtained from (adiabatic) quantum scattering calculations on both the  $V_{\text{sum}}$  and  $V_{\text{dif}}$  potentials. The theoretical results overestimate the degree of experimental RET, but both agree that elastic depolarisation is a minor channel in this system. It is interesting to note that electronic quenching of  $\text{CN(A)}$  by Ar is competitive with

RET [82]. The size of the quenching cross sections [83, 84], while not quite large enough to account for the difference between theory and experiment, is at least of a similar order to the differences observed. Costen and coworkers note that collisions extending into the attractive well of the PES must contribute to RET [25], and so it is plausible that at least some of the discrepancy between calculation and experiment could be attributed to quenching, as in the case of  $\text{OH(A)} + \text{Kr}$ .

The most recent results from Costen *et al.* concern state-to-state rotational energy transfer and disorientation [85]. Strong alternations, both in RET rate constants ( $k_{jj'}$ ) and disorientation parameters ( $a^{(1)}(j, j')$ ) are observed for even and odd  $\Delta j$ . These differences are between collisions which conserve and change the rotational parity — parity-conserving collisions tend to conserve orientation (positive  $a^{(1)}(j, j')$ ) and parity-changing collisions lead to more disorientation (near-zero, or negative  $a^{(1)}(j, j')$ ) [85]. Different dynamics in these two kinds of collisions result from the different terms of the PESs responsible. Even- $\lambda$  terms in the Legendre expansion of the PESs result mainly in parity-conserving collisions, and odd- $\lambda$  terms in parity-changing collisions [85–87]. Because the  $\text{CN(A)} + \text{Ar}$  system is near-homonuclear, even- $\lambda$  terms dominate, leading to a propensity to conserve parity [85] and hence the alternations seen in the state-to-state RET rate constants.

#### 4.8. Crossed-beam studies of $\text{NO(A)} + \text{Rg}$

In addition to the collisional depolarisation studies reviewed in section 4.3.1, which took place in a thermal bath of collision gas,  $\text{NO(A)} + \text{Rg}$  systems have also been investigated using a combined crossed molecular beam and theoretical study by the

groups of Costen, Chandler and Alexander [88–90]. This has looked at differential cross sections (DCSs) for  $\text{NO(A)} + \text{He}$  and  $\text{NO(A)} + \text{Ar}$  collisions [88, 89] and collision induced alignment in  $\text{NO(A)} + \text{Ne}$  [90], complementing the insight into these systems obtained from collisional depolarisation studies. Comparison can also be made with the related work on  $\text{NO(X)-Rg}$  collisions by Brouard and coworkers [91–99].

Experimental DCSs for  $\text{NO(A)} + \text{He}$  displayed excellent agreement with those from quantum scattering calculations [89], but, in the case of  $\text{NO(A)} + \text{Ar}$ , there were two sources of disagreement. The first of these, relating to the forward-scattered direction, can be explained as an experimental artifact caused by the background subtraction technique employed [89]. However, the other discrepancy – in the angular position of the rotational rainbow peaks – was found to be due to the description of the short-range anisotropy of the repulsive wall of the PES [89]. As  $\text{NO(A)} + \text{Ar}$  has a more attractive character than  $\text{NO(A)} + \text{He}$ , the description of the intermolecular potential is more difficult for this system; in addition, the collision energy was higher in the  $\text{NO(A)} + \text{Ar}$  collisions than for  $\text{NO(A)} + \text{He}$ , meaning that these experiments were more sensitive to the short-range repulsive regions of the PES [89].

A newer PES for  $\text{NO(A)} + \text{Ar}$  [29] was found to agree well with that of Kłos *et al.* [28] in the region of the global minimum, but was deeper in other configurations. The main difference was in the choice of basis set. The steeper  $V_{10}$  component in the new PES may help with the description of the short-range repulsion, and a comparison of calculations on the two potentials would help to pin down the factors responsible for the disagreement with experiment [89].

The most recent paper of Costen, Chandler and coworkers [90], investigated the angular momentum alignment of NO(A) induced by collisions with Ne. When resolved in scattering angle, the overall trend in this collision-induced alignment could be modelled using a classical hard-shell method, but the experimental data also displayed scattering angle-dependent oscillations that could only be reproduced using quantum scattering calculations [90]. This difference was attributed to the range of the repulsive interactions on the NO(A) + Ne PES; instead of a ‘hard’ shell, the true interaction is ‘softer’ in character and extends over a larger radius [28, 90].

## 5. Mechanism of depolarisation

### 5.1. Kinematic apse

For purely impulsive collisions between rigid bodies, it has been shown that the projection of  $\mathbf{j}$  onto the kinematic apse is conserved [100, 101], where the apse is defined as:

$$\mathbf{a} = \frac{\mathbf{k}' - \mathbf{k}}{|\mathbf{k}' - \mathbf{k}|} \quad (42)$$

where  $\mathbf{k}$  and  $\mathbf{k}'$  are the initial and final relative velocities, respectively. With  $m_a$  and  $m'_a$  representing the projection of  $\mathbf{j}$  and  $\mathbf{j}'$  respectively onto  $\mathbf{a}$ ,  $\Delta m_a = m'_a - m_a$  is the change in this projection, which should be zero for a purely impulsive collision. QCT (closed shell) histogram plots of  $\Delta m_a$  for  $N=2$  are shown in figure 21 for OH(A) under thermal conditions (top row) and superthermal conditions (middle row), and for NO(A) (bottom row). The three columns correspond to He (left), Ar (middle) and Kr (right). In all cases, the projection of  $\mathbf{j}$  onto the kinematic apse is conserved more for elastic depolarising trajectories (shown in blue) than inelastic trajectories



(shown in red). This is as expected, as RET is more likely to be accompanied by a large change in the direction of  $\mathbf{j}$  than elastic collisions. Note that, in this case, elastic depolarising trajectories are defined as those for which  $|\Delta j| \leq 0.5$  but  $\Delta K \geq 0.5$  [21].

The projection is most rigorously conserved in the case of  $\text{NO}(\text{A}) + \text{He}$  (bottom left panel), where the PES is almost purely repulsive, and most closely resembles that between a hard sphere and a hard ellipsoid. On going from He to Ar and Kr, the conservation of the projection becomes poorer as the PESs become more attractive. The well depth of the  $\text{OH}(\text{A}) + \text{He}$  and  $\text{NO}(\text{A}) + \text{Kr}$  PESs are comparable in magnitude, although better conservation is observed in  $\text{OH}(\text{A}) + \text{He}$  than  $\text{NO}(\text{A}) + \text{Kr}$ . However, the RET cross sections are smaller for  $\text{OH}(\text{A}) + \text{He}$  than  $\text{NO}(\text{A}) + \text{Kr}$ , and so the collisions are more likely to be impulsive. Again, the projection is less well conserved as the Rg gets heavier. Increasing the collision energy also results in the less conservation of the projection of  $\mathbf{j}$  onto the kinematic apse. As the collisions are more impulsive at higher collision energies, it would be expected that the conservation would be better. However, there is significantly more RET at higher collision energies. Therefore, to maintain the projection of  $\mathbf{j}$  onto the apse, the direction would have to change significantly. This would result in significant depolarisation. As already shown, collisions are less depolarising as the collision energy is increased, meaning the direction of  $\mathbf{j}$  does not change significantly. Consequently, the projection of  $\mathbf{j}$  onto the apse is not conserved as well as for lower collision energies.

## 5.2. Deflection functions ( $b$ vs $\theta$ )

The dependence of the scattering angle,  $\theta$ , on the impact parameter,  $b$  – *i.e.* the classical (closed shell) deflection function – is shown in figure 22 for OH(A) under thermal (300 K, top row) and superthermal (middle row) collision energies, and for (thermal) NO(A) (bottom row), in collisions with He (left column), Ar (middle column) and Kr (right column). The blue points correspond to elastic collisions and the red points inelastic collisions, and the initial state is  $N=2$ . The most impulsive behaviour is observed for NO(A) + He, where the scattering angle decreases as the impact parameter increases. This again reflects the almost purely repulsive nature of the NO(A) + He PES. On going from He to Ar and Kr, the PESs become more attractive, and this is reflected in the plots, with a clear ‘maximum’ (as the deflection angles are negative, this is in fact a minimum) observed in the case of NO(A) + Kr, where the Kr is sampling the attractive part of the potential.

The increased well depths for OH(A) + Ar and OH(A) + Kr lead to orbiting trajectories in both cases, where the radical and rare gas are trapped in a complex. These complexes can fall apart at any point in the rotation, and this leads the curved structure observed in the top middle and top right panels of the figure. As the collision energy is increased, there are no longer orbiting trajectories in OH(A) + Ar. The Ar still samples the attractive part of the PES, but is travelling too quickly to be trapped in a complex. However, even at the higher collision energy orbiting trajectories are still observed in OH(A) + Kr. This is due to the significant attractive nature of the PES (well depth  $\approx 6000\text{ cm}^{-1}$  [22]). The double band structure that can be most clearly seen in the OH(A) + Ar and OH(A) + Kr superthermal plots is due to

scattering off either end of the OH(A) molecule. This structure is more diffuse at thermal collision energies, due to the influence of the attractive part of the potential, and is not observable in the case of the more symmetric NO(A) molecule.

### 5.3. Opacity functions

The closed shell adiabatic QCT opacity functions are shown in figure 23 for  $N=2$  for OH(A) under thermal (top row) and superthermal (middle row) collision energies, and for (thermal) NO(A) (bottom row). The left hand column corresponds to He, the middle to Ar and the right to Kr. The probability of an inelastic or elastic collision,  $P^{(0)}(b)$ , is shown as the solid blue and red lines, respectively. In the classical case, these necessarily sum to unity. It should also be noted that the elastic opacity functions tend to one at large impact parameters as the elastic cross sections cannot be converged in the QCT calculations. Inelastic collisions are more probable in NO(A) than OH(A), due to the different moments of inertia associated with the two radicals which leads to a smaller rotational energy level spacing in NO(A) than OH(A). As the collision energy is increased and more rotational levels become accessible, inelastic collisions also become more probable in OH(A). However, the range of impact parameters over which RET occurs is smaller in OH(A) under both thermal and superthermal collision energies than in NO(A). This reflects the longer range of the NO(A) + Rg PESs compared to those for the OH(A) + Rgs.

The dashed lines in figure 23 show the extent to which collisions cause disalignment. These have been calculated using:

$$P^{(2)}(b) = P^{(0)}(b) \left(1 - a^{(2)}\right) \quad (43)$$

As  $a^{(2)}$  can be negative, it is possible for  $P^{(2)}(b)$  to be greater than one. It should also be noted that it is possible to converge the elastic values of  $P^{(2)}(b)$ , as there is a maximum impact parameter above which no elastic depolarisation occurs. For the NO(A) + Rg systems, collisions do not cause significant depolarisation. This is particularly the case for NO(A) + He, where collisions have been shown to be very impulsive. Depolarisation is also seen to be inefficient compared to RET in OH(A) + He under thermal conditions, although every collision in OH(A) + Ar and OH(A) + Kr leads to complete randomisation of the direction of  $\mathbf{j}$ . This efficient depolarisation is maintained over all impact parameters where RET occurs for OH(A) + Rg, whereas at larger impact parameters RET can occur in NO(A) + Rg without any depolarisation. Elastic depolarisation also plays a more significant role in the OH(A) + Rg systems under thermal conditions, and for the heavier rare gases elastic depolarisation occurs at larger impact parameters than RET. This suggests that unlike in OH(X) + Ar [11], elastic depolarisation is influenced by the long range part of the PES under thermal conditions. As the collision energy is increased for OH(A) + Rg, the collisions cause less depolarisation, and the observed trends start to resemble those seen in the NO(A) + Rg systems. This reflects the more impulsive nature of the collisions as the more repulsive core of the PES is sampled.

#### 5.4. TSH-QCT opacity functions

Figure 24 presents two-state closed shell TSH-QCT opacity functions,  $P(b)$ , for inelastic collisions and collisions leading to surface hopping (*i.e.* electronic quenching), and also  $P^{(2)}(b)$  for elastic disalignment (equation (43)). Opacity functions are shown

for  $N = 2, 5$  and  $8$  for the  $\text{OH(A)} + \text{Kr}$  system. In this way, it is possible to compare the ranges at which these processes can take place.

In the left-hand panel for  $N = 2$ , it is clear that elastic depolarisation can take place at larger impact parameters than RET or quenching, whereas surface-hopping has a similar range to that of inelastic collisions. As  $N$  increases, although appreciable surface-hopping no longer takes place, the difference in range between inelastic and elastic depolarising collisions increases, supporting the conclusion that these processes are influenced by different regions of features of the potential. The presence of quenching thus suppresses RET, which is in direct competition with it. There is less competition between quenching and elastic depolarisation, which can take place at longer range. This explains why the adiabatic QCT theory does a good job of modelling elastic depolarisation for  $\text{OH(A)} + \text{Kr}$ , but has more trouble reproducing experimental inelastic depolarisation due to the competing non-adiabatic pathway.

## 6. Depolarisation in larger systems

### 6.1. $\text{NO(A)} + \text{N}_2$ and $\text{NO(A)} + \text{O}_2$ , 300 K

The total disalignment cross sections have been recorded for  $\text{NO(A)} + \text{N}_2$  and  $\text{NO(A)} + \text{O}_2$ , and these are presented in figure 25. The left hand panel of the figure shows the results for  $\text{NO(A)} + \text{N}_2$  and the middle panel  $\text{NO(A)} + \text{O}_2$ . The low  $N$  data was recorded using hyperfine quantum beat spectroscopy (shown as open triangles), and the high  $N$  data using Zeeman quantum beat spectroscopy (filled triangles). For  $N=5$ , where it is possible to record the data using both hyperfine and Zeeman quantum beats, the cross sections obtained from each method are in good agreement.

The depolarisation cross sections again fall with increasing  $N$ , as was the case with the  $\text{NO(A)} + \text{Rg}$  systems above.

The masses of  $\text{N}_2$  and  $\text{O}_2$  are similar to that of Ar, meaning the kinematics of the systems will not be significantly different. Therefore any differences in the depolarisation is likely to be brought about by differences in the PES. Snow *et al.* [102] measured an elastic depolarisation cross-section for  $N=4$  for  $\text{NO(A)} + \text{N}_2$  of less than  $1 \text{ \AA}^2$ . This is similar to what is observed in the  $\text{NO(A)} + \text{Rg}$  systems discussed previously, where elastic depolarisation makes only a small contribution to the total depolarisation cross-section. Snow *et al.* concluded that the rate of elastic depolarisation is most dependent on the size of the multipole moments, and is greatest for molecules with a permanent dipole moment. It therefore seems reasonable to assume that the elastic depolarisation cross-section for  $\text{NO(A)} + \text{O}_2$  will be similarly small. RET cross sections have also been measured for  $\text{NO(A)} + \text{N}_2$  and  $\text{NO(A)} + \text{O}_2$  by Lee *et al.* [103]. These are of a comparable magnitude to those obtained for  $\text{NO(A)} + \text{He}$  from the QCT calculations. Therefore the RET cross sections are smaller for  $\text{NO(A)} + \text{N}_2$  and  $\text{NO(A)} + \text{O}_2$  than  $\text{NO(A)} + \text{Ar}$ . As the total depolarisation cross sections for both  $\text{NO(A)} + \text{N}_2$  and  $\text{NO(A)} + \text{O}_2$  are similar to the total for  $\text{NO(A)} + \text{Ar}$ , shown in the right panel of the figure, and the elastic depolarisation cross sections make a similarly small contribution in both cases, it can be deduced that collisions of  $\text{NO(A)} + \text{N}_2$  and  $\text{NO(A)} + \text{O}_2$  cause more depolarisation than collisions of  $\text{NO(A)}$  with Ar. Therefore it is likely that the PESs for  $\text{NO(A)} + \text{N}_2$  and  $\text{NO(A)} + \text{O}_2$  are more anisotropic than that for  $\text{NO(A)} + \text{Ar}$ .

## 6.2. OH(A) + H<sub>2</sub>, 300 K

RET and disorientation cross sections have been measured experimentally for OH(A) + H<sub>2</sub> under thermal conditions, and the results are presented in figure 26. These results are a subset of the more extensive data set currently in preparation for publication.

Of the systems considered in the previous section, OH(A) + H<sub>2</sub> is most kinematically similar to OH(A) + He, but the PES [31] is significantly more anisotropic, and therefore resembles more those for OH(A) with the heavier rare gases. Therefore, to determine the role of these two factors, the cross sections can be compared with those for OH(A) + He and OH(A) + Ar.

The RET cross sections for OH(A) + H<sub>2</sub> do not appear to have much of a dependence on  $N$ , in contrast to those for OH(A) + He or Ar. This is due to the very strong attractive wells in the OH(A) + H<sub>2</sub> PES [31], which result in significant torques being applied to OH(A) even at long range. In this respect, OH(A) + H<sub>2</sub> behaves more like the heavier rare gas systems, such as OH(A) + Kr.

As can be seen, the OH(A) + H<sub>2</sub> total depolarisation cross sections are larger than those obtained for OH(A) + He, showing that the increased anisotropy of the PES leads to increased disorientation cross sections. Their magnitude is similar to, or larger than, that of the RET cross sections, indicating that inelastic collisions are very depolarising. However, they are smaller than those observed in OH(A) + Ar, showing that the light mass of the H<sub>2</sub> is also a factor in depolarisation.

Considering the elastic disorientation cross sections, inelastic depolarisation appears to be the major contributor to the total, with the behaviour of OH(A) + H<sub>2</sub>

being more similar to  $\text{OH(A)} + \text{He}$  than  $\text{OH(A)} + \text{Ar}$ .

It should be emphasized that electronic quenching and reaction (to form  $\text{H} + \text{H}_2\text{O}$ ) are also major channels in the  $\text{OH(A)} + \text{H}_2$  system [32, 65], and there are many seams of conical intersections between the excited and ground state potentials [104, 105]. Competition between these non-adiabatic pathways and RET or collisional depolarisation could have an effect on the cross sections displayed here.

## 7. Conclusions and future work

The main comparison in this paper is between the behaviour of  $\text{OH(A)}$  and  $\text{NO(A)}$  in collisions.  $\text{NO(A)} + \text{Rg}$  collisions are largely impulsive, like the collisions of ground state  $\text{NO(X)}$  [24], as evidenced by the high degree of conservation of the projection of  $\mathbf{j}$  on the kinematic apse. This is due to the weakly attractive, nearly isotropic potentials on which the collisions take place. Moving from the almost purely repulsive  $\text{NO(A)} + \text{He}$  system to heavier colliders, the attractive forces get stronger, but are not on the same scale as  $\text{OH(A)} + \text{Rg}$  interactions. Collisions of  $\text{NO(A)}$  with rare gases demonstrate a high degree of rotational energy transfer, but are inefficient at destroying the polarisation of  $\mathbf{j}$ . It is kinematically difficult to change the plane or sense of rotation of a heavy, near-homonuclear rotor such as  $\text{NO}$ , more so in the case of a light collider such as  $\text{He}$  than for a heavier collider. Elastic depolarisation is very inefficient – collisions in which the forces between  $\text{NO(A)}$  and the collider are strong enough to cause depolarisation of  $\mathbf{j}$  are likely to result in a change in its magnitude, too. Inelastic depolarisation dominates due to the competition between elastic depolarisation and RET across the whole PES.



In contrast,  $\text{OH(A)} + \text{Rg}$  systems tend to have much more anisotropic potentials with stronger attractive forces. Indeed,  $\text{OH(A)} + \text{Ar}$  and  $\text{OH(A)} + \text{Kr}$  demonstrate orbiting collisions, where the collision complex is trapped in the deep  $\text{HO-Rg}$  well for a number of rotational periods. A single collision can effectively randomise the direction of  $\mathbf{j}$ , leading to efficient depolarisation. Interestingly, despite the collisions being nowhere near impulsive, there is still a propensity to conserve the projection of  $\mathbf{j}$  on the kinematic apse. Elastic depolarisation is an important contribution to the total, making up a larger fraction of the whole at higher  $N$  as RET becomes less efficient. This is because, in heavier  $\text{OH(A)} + \text{Rg}$  systems, elastic depolarisation extends to longer range than RET, in contrast to  $\text{NO(A)}$  where they compete everywhere. This is also unlike the behaviour observed in  $\text{OH(X)}$  [24]. At higher, superthermal collision energies,  $\text{OH(A)} + \text{Rg}$  systems begin to display behaviour more similar to  $\text{NO(A)} + \text{Rg}$  due to the attractive part of the potential having less influence.

$\text{CN(A)} + \text{Ar}$  displays similar behaviour to  $\text{NO(A)} + \text{Ar}$  due to the weakly attractive potential and identical kinematics. Elastic depolarisation is found to be inefficient relative to RET processes. However, comparisons are complicated by  $\text{CN(A)}$  being a  $^2\Pi$  state.

For most of the systems reviewed here, adiabatic QCT calculations do an excellent job at modelling the experimental quantities measured. However,  $\text{OH(A)} + \text{Kr}$  displays significant electronic quenching, which competes with RET and inelastic depolarisation at low  $N$ . The same features of the PES (the deep  $\text{HO-Kr}$  well) are responsible for quenching and electronically adiabatic, rotationally inelastic processes, meaning that the presence of quenching acts to suppress the inelastic depolarisa-

tion cross sections. As elastic depolarisation takes place at longer range, there is less competition with quenching and it can be better predicted by adiabatic theory. The inclusion of non-adiabatic effects through TSH-QCT models helps to account for these competing channels, and yields improved agreement with experiment.

A natural extension of the work presented here is to study the OH(A)-Xe system, which displays a larger degree of electronic quenching than OH(A) + Kr. This work is currently underway in our laboratory. In addition, full quasi-classical and quantum scattering calculations of the three-state ( $1A'$ ,  $1A''$  and  $2A'$ ) problem would be highly desirable for comparison with the approximate semiclassical methods used here.

### Acknowledgements

The authors would like to thank D. Herráez-Aguilar for his contributions to the trajectory surface-hopping results presented here, and Y.-P. Chang, C. J. Eyles, G. McCrudden and S. A. Seamons for their work on the experimental and QCT studies included in this review. The potential energy surfaces, and some of the QM scattering results, were calculated by J. Kłos, M. H. Alexander and P. J. Dagdigian. Helpful discussions with K. G. McKendrick, M. Costen, J. Kłos, M. H. Alexander, M. I. Lester, and P. J. Dagdigian are gratefully acknowledged. The support of the UK EPSRC (to M.B. *via* Programme Grant No. EP/G00224X/1), the EU (to M.B. *via* FP7 EU People ITN project 238671), and the Spanish Ministry of Science and Innovation (to F.J.A. *via* grants CTQ2008-02578/BQU, CSD2009-00038, and CTQ2012-37404-C02) are gratefully acknowledged.

**References**

- [1] H. J. Crichton, M. L. Costen, and K. G. McKendrick, *J. Chem. Phys.* **119**, 9461 (2003).
- [2] M. L. Costen, H. J. Crichton, and K. G. McKendrick, *J. Chem. Phys.* **120**, 7910 (2004).
- [3] M. Brouard, A. Bryant, I. Burak, F. Quadrini, S. Marinakis, I. A. Garcia, and C. Vallance, *Mol. Phys.* **103**, 1693 (2005).
- [4] S. Marinakis, G. Paterson, J. Kłos, M. L. Costen, and K. G. McKendrick, *Phys. Chem. Chem. Phys.* **9**, 4414 (2007).
- [5] J. Kłos, M. H. Alexander, M. Brouard, C. J. Eyles, and F. J. Aoiz, *J. Chem. Phys.* **129**, 054301 (2008).
- [6] S. Marinakis, G. Paterson, G. Richmond, M. Rockingham, M. L. Costen, and K. G. McKendrick, *J. Chem. Phys.* **128**, 021101 (2008).
- [7] G. Paterson, S. Marinakis, M. L. Costen, K. G. McKendrick, J. Kłos, and R. Tobota, *J. Chem. Phys.* **129**, 074304 (2008).
- [8] G. Paterson, S. Marinakis, J. Kłos, M. L. Costen, and K. G. McKendrick, *Phys. Chem. Chem. Phys.* **11**, 8804 (2009).
- [9] G. Paterson, S. Marinakis, M. L. Costen, and K. G. McKendrick, *Phys. Chem. Chem. Phys.* **11**, 8813 (2009).
- [10] P. J. Dagdigian and M. H. Alexander, *J. Chem. Phys.* **130**, 094303 (2009).
- [11] P. J. Dagdigian and M. H. Alexander, *J. Chem. Phys.* **130**, 164315 (2009).
- [12] P. J. Dagdigian and M. H. Alexander, *J. Chem. Phys.* **130**, 204304 (2009).
- [13] F. J. Aoiz, M. Brouard, C. J. Eyles, J. Kłos, and M. P. de Miranda, *J. Chem. Phys.* **130**, 044305 (2009).
- [14] M. Brouard, A. Bryant, Y. P. Chang, R. Cireasa, C. J. Eyles, A. M. Green, S. Marinakis, F. J. Aoiz, and J. Kłos, *J. Chem. Phys.* **130**, 044306 (2009).
- [15] M. Brouard, H. Chadwick, Y. P. Chang, R. Cireasa, and C. J. Eyles, *Physica Scripta* **80**, 048120 (2009).

- [16] M. Brouard, H. Chadwick, Y. P. Chang, R. Cireasa, C. J. Eyles, A. O. L. Via, N. Screen, F. J. Aoiz, and J. Kłos, *J. Chem. Phys.* **131**, 104307 (2009).
- [17] M. L. Costen, R. Livingstone, K. G. McKendrick, G. Paterson, M. Brouard, H. Chadwick, Y. P. Chang, C. J. Eyles, F. J. Aoiz, and J. Kłos, *J. Phys. Chem. A* **113**, 15156 (2009).
- [18] I. Ballingall, M. F. Rutherford, K. G. McKendrick, and M. L. Costen, *Mol. Phys.* **108**, 847 (2010).
- [19] L. Ma, M. H. Alexander, and P. J. Dagdigian, *J. Chem. Phys.* **134**, 154307 (2011).
- [20] M. Brouard, H. Chadwick, C. J. Eyles, F. J. Aoiz, and J. Kłos, *J. Chem. Phys.* **135**, 084305 (2011).
- [21] M. Brouard, H. Chadwick, Y. P. Chang, C. J. Eyles, F. J. Aoiz, and J. Kłos, *J. Chem. Phys.* **135**, 084306 (2011).
- [22] H. Chadwick, M. Brouard, Y. P. Chang, C. J. Eyles, T. Perkins, S. A. Seamons, J. Kłos, M. H. Alexander, and F. J. Aoiz, *J. Chem. Phys.* **137**, 154305 (2012).
- [23] G. Paterson, M. L. Costen, and K. G. McKendrick, *Mol. Phys.* **109**, 2565 (2011).
- [24] G. Paterson, M. L. Costen, and K. G. McKendrick, *Int. Rev. Phys. Chem.* **31**, 69 (2012).
- [25] S. J. McGurk, K. G. McKendrick, M. L. Costen, D. I. G. Bennett, J. Kłos, M. H. Alexander, and P. J. Dagdigian, *J. Chem. Phys.* **136**, 164306 (2012).
- [26] H. Chadwick, M. Brouard, Y. P. Chang, C. J. Eyles, G. McCrudden, T. Perkins, S. A. Seamons, J. Kłos, M. H. Alexander, P. J. Dagdigian, D. Herráez-Aguilar, and F. J. Aoiz, *J. Chem. Phys.* **140**, In press (2014).
- [27] T. Perkins, D. Herráez-Aguilar, M. Brouard, G. McCrudden, F. J. Aoiz and J. Kłos, in preparation (2014).
- [28] J. Kłos, M. H. Alexander, R. Hernández-Lamoneda, and T. G. Wright, *J. Chem. Phys.* **129**, 244303 (2008).
- [29] H. Cybulski and B. Fernández, *J. Phys. Chem. A* **116**, 7319 (2012).
- [30] J. H. Lehman, M. I. Lester, J. Kłos, M. H. Alexander, P. J. Dagdigian, D. Herráez-

- Aguilar, F. J. Aoiz, M. Brouard, H. Chadwick, T. Perkins, and S. A. Seamons, J. Phys. Chem. A **117**, 13481 (2013).
- [31] B. Fu, E. Kamarchik, and J. M. Bowman, J. Chem. Phys. **133**, 164306 (2010).
- [32] L. P. Dempsey, C. Murray, and M. I. Lester, J. Chem. Phys. **127**, 151101 (2007).
- [33] F. J. Aoiz, V. Sáez-Rábanos, B. Martínez-Haya, and T. González-Lezana, J. Chem. Phys. **123**, 094101 (2005).
- [34] M. P. de Miranda and F. J. Aoiz, Phys. Rev. Lett. **93**, 083201 (2004).
- [35] M. P. de Miranda, F. J. Aoiz, M. Brouard, and V. Sáez-Rábanos, J. Chem. Phys. **121**, 9830 (2004).
- [36] M. H. Alexander and S. L. Davis, J. Chem. Phys. **78**, 6754 (1983).
- [37] G. C. Corey, M. H. Alexander, and J. Schaefer, J. Chem. Phys. **85**, 2726 (1986).
- [38] G. C. Corey and F. R. McCourt, J. Phys. Chem. **87**, 2723 (1983).
- [39] G. C. Corey and A. D. Smith, J. Chem. Phys. **83**, 5663 (1985).
- [40] K. H. Gericke, S. Klee, F. J. Comes, and R. N. Dixon, J. Chem. Phys. **85**, 4463 (1986).
- [41] A. U. Grunewald, K. H. Gericke, and F. J. Comes, J. Chem. Phys. **89**, 345 (1988).
- [42] R. N. Dixon, J. Nightingale, C. M. Western, and X. Yang, Chem. Phys. Lett. **151**, 328 (1988).
- [43] K. H. Gericke, H. G. Gläser, C. Maul, and F. J. Comes, J. Chem. Phys. **92**, 411 (1990).
- [44] M. P. Docker, A. Hodgson, and J. P. Simons, Faraday Discuss. Chem. Soc. **82**, 25 (1986).
- [45] J. August, M. Brouard, M. P. Docker, A. Hodgson, C. J. Milne, and J. P. Simons, Ber. Bunsenges. Phys. Chem. **92**, 264 (1988).
- [46] M. Brouard, M. T. Martinez, C. J. Milne, and J. P. Simons, Chem. Phys. Lett. **165**, 423 (1990).
- [47] A. J. Alexander, Phys. Rev. A **66**, 060702 (2002).
- [48] A. J. Alexander, J. Chem. Phys. **118**, 6234 (2003).

- [49] J. J. ter Meulen, W. A. Majewski, W. L. Meerts, and A. Dymanus, *Chem. Phys. Lett.* **94**, 25 (1983).
- [50] J. J. ter Meulen, W. Ubachs, and A. Dymanus, *Chem. Phys. Lett.* **129**, 533 (1986).
- [51] P. Lebow, F. Raab, and H. Metcalf, *Phys. Rev. Lett.* **42**, 85 (1979).
- [52] F. Raab, T. Bergeman, D. Lieberman, and H. Metcalf, *Optics Lett.* **5**, 427 (1980).
- [53] F. Raab, T. Bergeman, D. Lieberman, and H. Metcalf, *Phys. Rev. A* **24**, 3120 (1981).
- [54] J. Xin, I. Ionescu, D. Kuffel, and S. A. Reid, *Chem. Phys.* **291**, 61 (2003).
- [55] P. J. Brucat and R. N. Zare, *J. Chem. Phys.* **78**, 100 (1983).
- [56] P. J. Brucat and R. N. Zare, *J. Chem. Phys.* **81**, 2562 (1984).
- [57] L. Rubio-Lago, D. Sofikitis, A. Koubenakis, and T. P. Rakitzis, *Phys. Rev. A* **74**, 042503 (2006).
- [58] A. J. Orr-Ewing and R. N. Zare, *Ann. Rev. of Phys. Chem.* **45**, 315 (1994).
- [59] A. U. Grunewald, K. H. Gericke, and F. J. Comes, *Chem. Phys. Lett.* **132**, 121 (1986).
- [60] M. Baba, M. Brouard, S. P. Rayner, and J. P. Simons, *Chem. Phys. Lett.* **220**, 411 (1994).
- [61] HIBRIDON is a package of programs for the time-independent quantum treatment of inelastic collisions and photodissociation written by M. H. Alexander, D. Manolopoulos, H.-J. Werner, and B. Follmeg, with contributions by P. F. Vohralik, D. Lemoine, G. Corey, R. Gordon, B. Johnson, T. Orlikowski, A. Berning, A. Degli-Esposti, C. Rist, P. Dagdigian, B. Pouilly, G. van der Sanden, M. Yang, F. de Weerd, S. Gregurick, and J. Klos.
- [62] D. E. Manolopoulos, *J. Chem. Phys.* **85**, 6425 (1986).
- [63] M. H. Alexander and D. E. Manolopoulos, *J. Chem. Phys.* **86**, 2044 (1987).
- [64] F. J. Aoiz, J. E. Verdasco, V. J. Herrero, V. S. Rábanos, and M. H. Alexander, *J. Chem. Phys.* **119**, 5860 (2003).
- [65] B. L. Hemming, D. R. Crosley, J. E. Harrington, and V. Sick, *J. Chem. Phys.* **115**, 3099 (2001).
- [66] J. C. Tully and R. K. Preston, *J. Chem. Phys.* **55**, 562 (1971).

- [67] J. C. Tully, *J. Chem. Phys.* **93**, 1061 (1990).
- [68] L. Bañares, F. J. Aoiz, P. Honvault, B. Busserly-Honvault, and J. M. Launay, *J. Chem. Phys.* **118**, 565 (2003).
- [69] L. Bonnet and J. C. Rayez, *Chem. Phys. Lett.* **397**, 106 (2004).
- [70] A. Jörg, A. D. Esposti, and H. J. Werner, *J. Chem. Phys.* **93**, 8757 (1990).
- [71] A. Jörg, U. Meier, and K. Kohse-Höinghaus, *J. Chem. Phys.* **93**, 6453 (1990).
- [72] R. K. Lengel and D. R. Crosley, *J. Chem. Phys.* **67**, 2085 (1977).
- [73] A. D. Esposti and H. J. Werner, *J. Chem. Phys.* **93**, 3351 (1990).
- [74] T. Imajo, K. Shibuya, and K. Obi, *Chem. Phys. Lett.* **137**, 139 (1987).
- [75] T. Ebata, Y. Anezaki, M. Fujii, N. Mikami, and M. Ito, *Chem. Phys.* **84**, 151 (1984).
- [76] P. H. Paul, J. L. Durant, J. A. Gray, and M. R. Furlanetto, *J. Phys. Chem* **102**, 8378 (1995).
- [77] K. L. Steffens and D. R. Crosley, *J. Chem. Phys.* **112**, 9427 (2000).
- [78] E. A. Brinkman and D. R. Crosley, *J. Phys. Chem. A* **108**, 8084 (2004).
- [79] A. Alagappan, I. Ballingall, M. L. Costen, and K. G. McKendrick, *J. Chem. Phys.* **126**, 041103 (2007).
- [80] M. H. Alexander, *Chem. Phys.* **92**, 337 (1985).
- [81] M. H. Alexander, X. Yang, P. J. Dagdigian, A. Berning, and H. J. Werner, *J. Chem. Phys.* **112**, 781 (2000).
- [82] J. H. Guo, A. Ali, and P. J. Dagdigian, *J. Chem. Phys.* **85**, 7098 (1986).
- [83] D. H. Katayama, T. A. Miller, and V. E. Bondybey, *J. Chem. Phys.* **71**, 1662 (1979).
- [84] Y. Huang, R. Lu, and J. B. Halpern, *Appl. Opt.* **32**, 981 (1993).
- [85] S. J. McGurk, K. G. McKendrick, M. L. Costen, M. H. Alexander, and P. J. Dagdigian, *J. Chem. Phys.* **139**, 124304 (2013).
- [86] M. H. Alexander, *J. Chem. Phys.* **76**, 5974 (1982).
- [87] P. J. Dagdigian, M. H. Alexander, and K. Liu, *J. Chem. Phys.* **91**, 839 (1989).
- [88] J. J. Kay, G. Paterson, M. L. Costen, K. E. Strecker, K. G. McKendrick, and D. W. Chandler, *J. Chem. Phys.* **134**, 091101 (2011).

- [89] J. J. Kay, J. D. Steill, J. Klos, G. Paterson, M. L. Costen, K. E. Strecker, K. G. McKendrick, M. H. Alexander, and D. W. Chandler, *Mol. Phys.* **110**, 1693 (2012).
- [90] J. D. Steill, J. J. Kay, G. Paterson, T. R. Sharples, J. Klos, M. L. Costen, K. E. Strecker, K. G. McKendrick, M. H. Alexander, and D. W. Chandler, *J. Phys. Chem. A* **117**, 8163 (2013).
- [91] J. Klos, F. J. Aoiz, J. E. Verdasco, M. Brouard, S. Marinakis, and S. Stolte, *J. Chem. Phys.* **127**, 031102 (2007).
- [92] F. J. Aoiz, J. E. Verdasco, M. Brouard, J. Klos, S. Marinakis, and S. Stolte, *J. Phys. Chem. A* **113**, 14636 (2009).
- [93] C. J. Eyles, M. Brouard, C. H. Yang, J. Klos, F. J. Aoiz, A. Gijsbertsen, A. E. Wiskerke, and S. Stolte, *Nature Chemistry* **3**, 597 (2011).
- [94] C. J. Eyles, M. Brouard, H. Chadwick, B. Hornung, B. Nichols, C. H. Yang, J. Klos, F. J. Aoiz, A. Gijsbertsen, A. E. Wiskerke, and S. Stolte, *Phys. Chem. Chem. Phys.* **14**, 5403 (2012).
- [95] C. J. Eyles, M. Brouard, H. Chadwick, F. J. Aoiz, J. Klos, A. Gijsbertsen, X. Zhang, and S. Stolte, *Phys. Chem. Chem. Phys.* **14**, 5420 (2012).
- [96] J. Klos, F. J. Aoiz, M. Menéndez, M. Brouard, H. Chadwick, and C. J. Eyles, *J. Chem. Phys.* **137**, 014312 (2012).
- [97] M. Brouard, H. Chadwick, C. J. Eyles, B. Hornung, B. Nichols, F. J. Aoiz, P. G. Jambrina, S. Stolte, and M. P. de Miranda, *J. Chem. Phys.* **138**, 104309 (2013).
- [98] M. Brouard, H. Chadwick, C. J. Eyles, B. Hornung, B. Nichols, F. J. Aoiz, P. G. Jambrina, and S. Stolte, *J. Chem. Phys.* **138**, 104310 (2013).
- [99] M. Brouard, H. Chadwick, C. J. Eyles, B. Hornung, B. Nichols, J. M. Scott, F. J. Aoiz, J. Klos, S. Stolte, and X. Zhang, *Mol. Phys.* **111**, 1759 (2013).
- [100] V. Khare, D. J. Kouri, and D. K. Hoffman, *J. Chem. Phys.* **74**, 2275 (1981).
- [101] D. K. Hoffman, J. W. Evans, and D. J. Kouri, *J. Chem. Phys.* **80**, 144 (1984).
- [102] L. D. Snow, R. N. Compton, and J. C. Miller, *J. Chem. Phys.* **88**, 1652 (1988).
- [103] S. Lee, J. Luque, J. Reppel, A. Brown, and D. R. Crosley, *J. Chem. Phys.* **121**, 1373



(2000).

[104] B. C. Hoffman and D. R. Yarkony, *J. Chem. Phys.* **113**, 10091 (2000).

[105] E. Kamarchik, B. Fu, and J. M. Bowman, *J. Chem. Phys.* **132**, 091102 (2010).

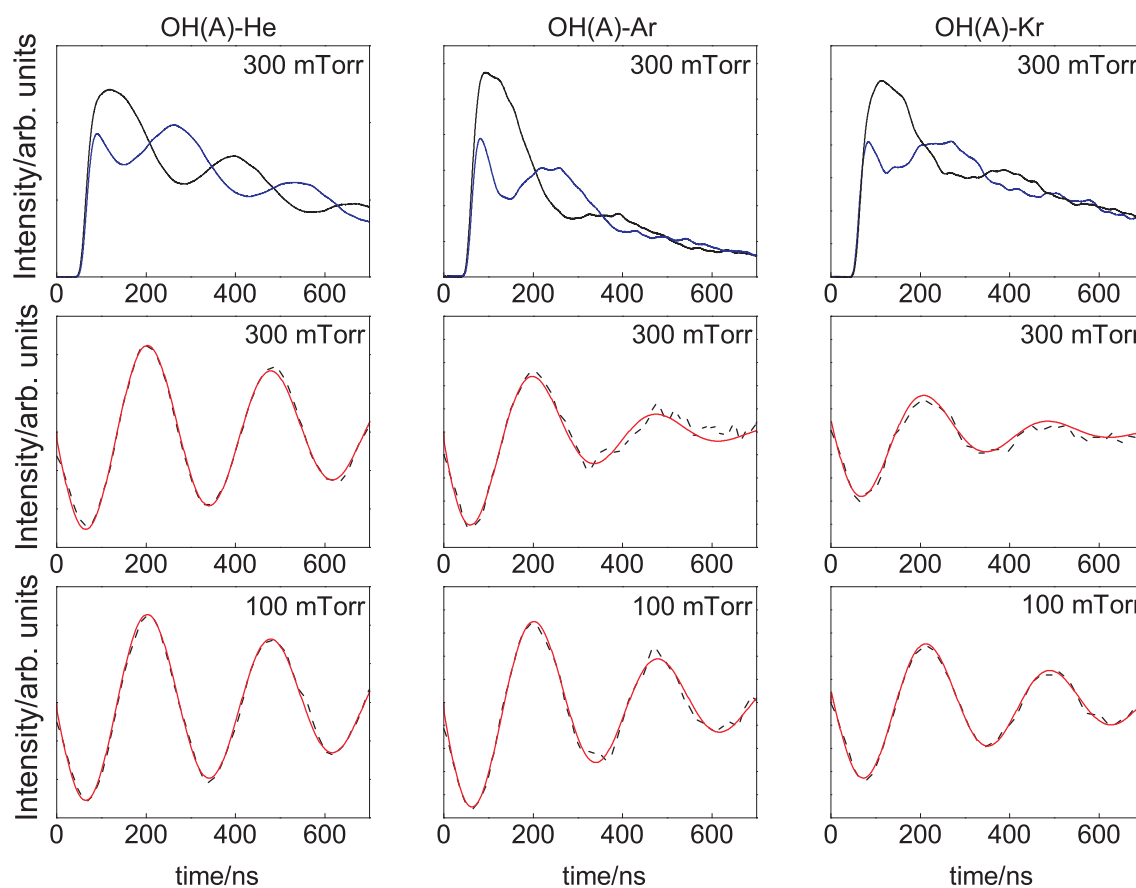


Figure 1. Top row: Typical orientation fluorescence decays recorded using Zeeman quantum beat spectroscopy for thermal (300 K) OH(A) with He (left column), Ar (middle column) and Kr (right column) following  $R_{22}(7)$  excitation. Middle and bottom row: The quantum beats (black dashed line) and the fit to the data (red solid line) at 300 mTorr (middle row) and 100 mTorr (bottom row).

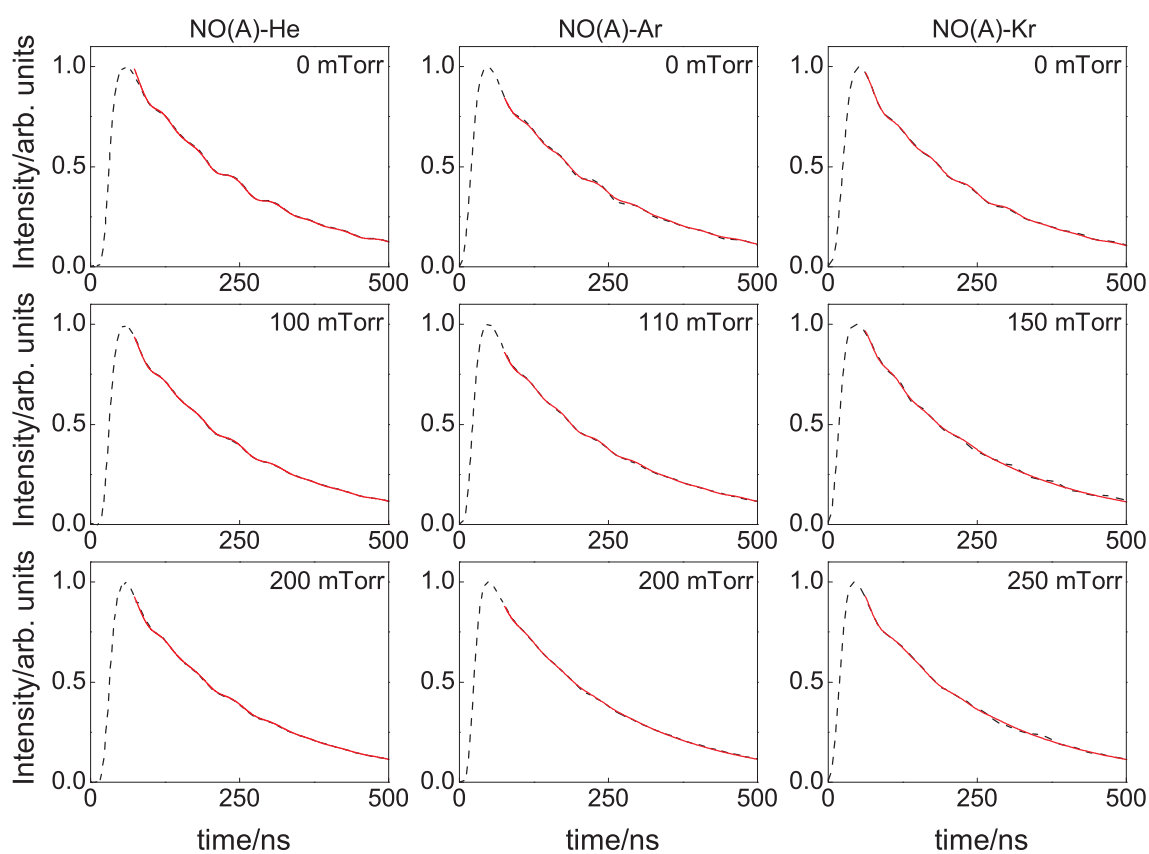


Figure 2. Typical fluorescence decays (300 K experiments) recorded using hyperfine quantum beat spectroscopy (black dashed line) and the fit to the data (red solid line) for NO(A) with He (left column), Ar (middle column) and Kr (right column) following  $S_{21}(0)$  excitation.

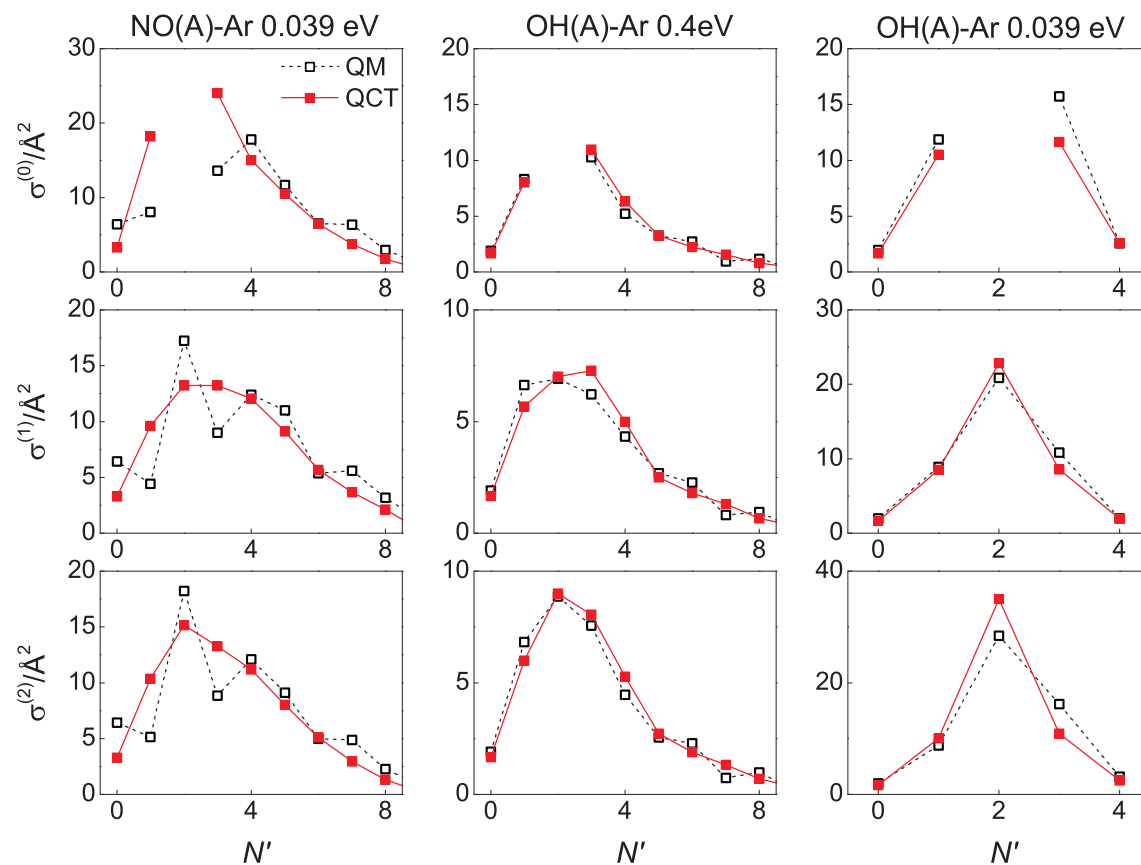


Figure 3. Comparison of closed shell, fixed collision energy QCT (solid squares) and QM (open squares) state-to-state RET (top panels), disorientation (middle panels) and disalignment (bottom panels) cross sections for NO(A) + Ar (0.039 eV, left column), superthermal OH(A) + Ar (0.4 eV, middle column) and thermal OH(A) + Ar (0.039 eV, right column) for initial  $N=2$  resolved in  $N'$ .

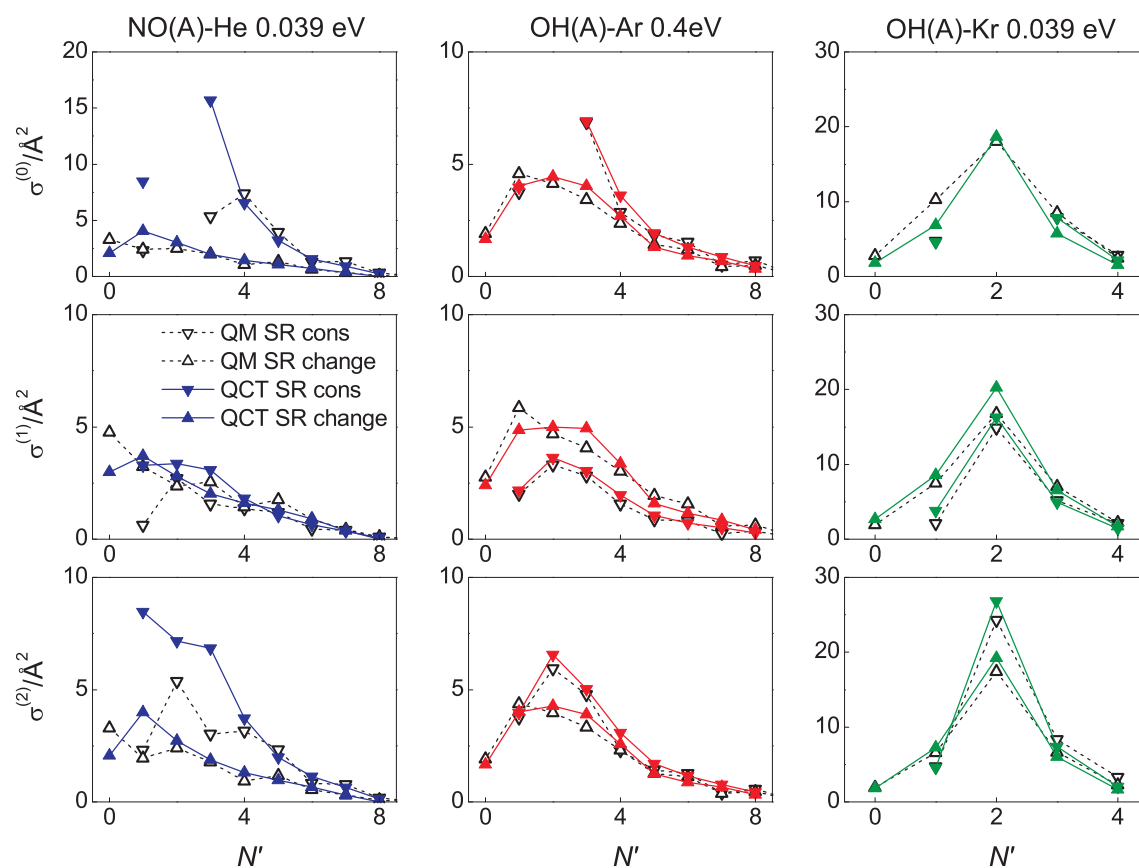


Figure 4. Comparison of open shell, fixed collision energy QCT (solid triangles) and QM (open triangles) state-to-state RET (top panels), disorientation (middle panels) and disalignment (bottom panels) cross sections for NO(A) + He (0.039 eV, left column), superthermal OH(A) + Ar (0.4 eV, middle column) and thermal OH(A) + Kr (0.039 eV, right column) for initial  $N=2$ ,  $j = 1.5$  resolved in  $N'$ . The downward pointing triangles show the cross sections for transitions which conserve the initial spin-rotation state ( $j' = N - S$ ) and the upward pointing triangles those which change the initial spin-rotation state ( $j' = N + S$ ).

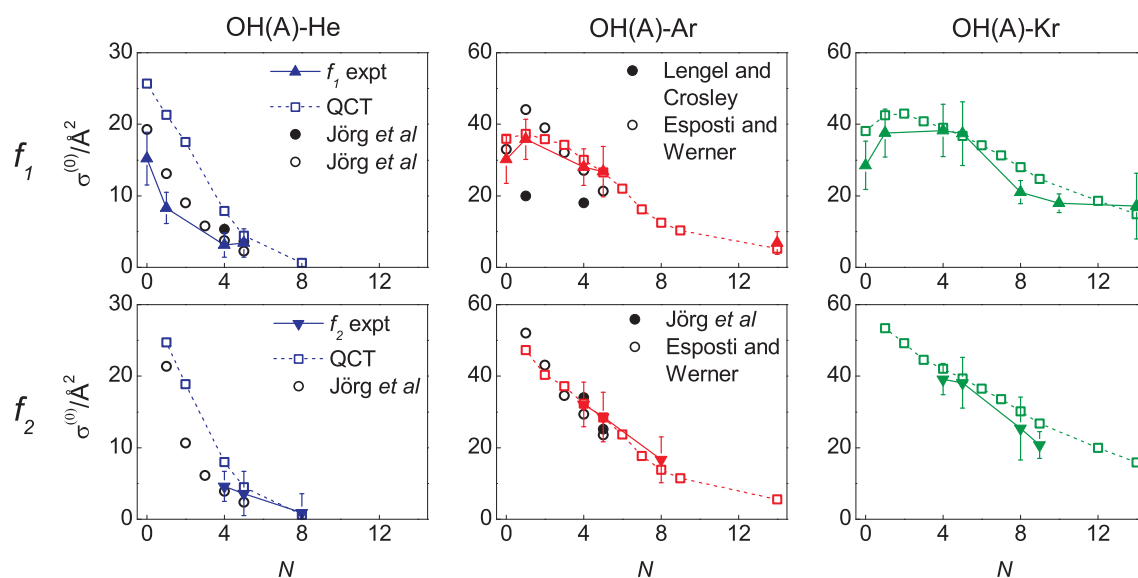


Figure 5. Comparison of thermally averaged experimental (300 K, triangles) and fixed energy QCT (0.039 eV, squares) total RET cross sections for the  $f_1$  (top row) and  $f_2$  (bottom row) spin rotation levels for OH(A) + He (left column), OH(A) + Ar (middle column) and OH(A) + Kr (right column). The RET data are summed over all final states ( $j' \neq j$ ), but are resolved in initial rotational state. For OH(A) + He, theoretical cross sections by Jörg *et al.* [70] are shown as open circles, and experimental results by Jörg *et al.* [71] are shown as solid circles. Previous experimental results for the  $f_2$  spin-rotation level by Lengel and Crosley [72] for OH(A) + Ar are shown as solid circles in the bottom panel, as are results obtained by Jörg *et al.* [71] for the  $f_1$  spin rotation level in the top panel. Theoretical cross sections by Esposti and Werner [73] are shown as open circles for both spin-rotation levels.

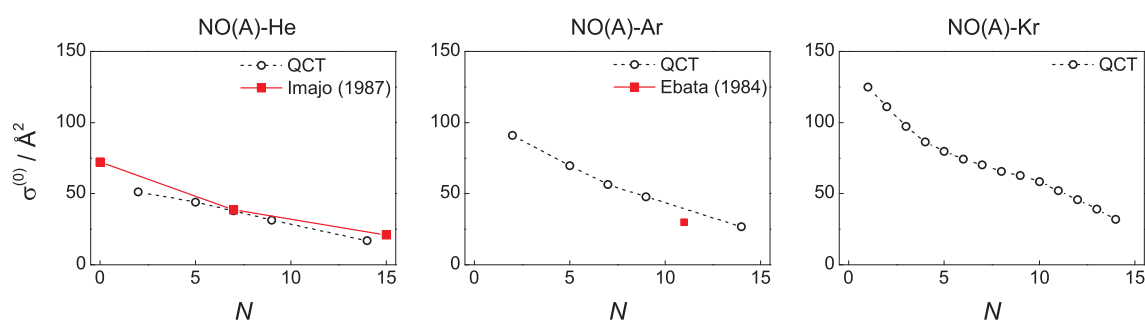


Figure 6. Fixed energy (0.039 eV) QCT total RET cross sections for NO(A) with He (left column), Ar (middle column) and Kr (right column). The RET data are summed over all final states ( $j' \neq j$ ), but are resolved in initial rotational state. Red squares show experimental results from Imajo *et al.* [74] for NO(A) + He and Ebata *et al.* [75] for NO(A) + Ar. All QCT cross sections are for the  $f_2$  spin-rotation level; the spin-rotation level used in the experimental data was not specified.

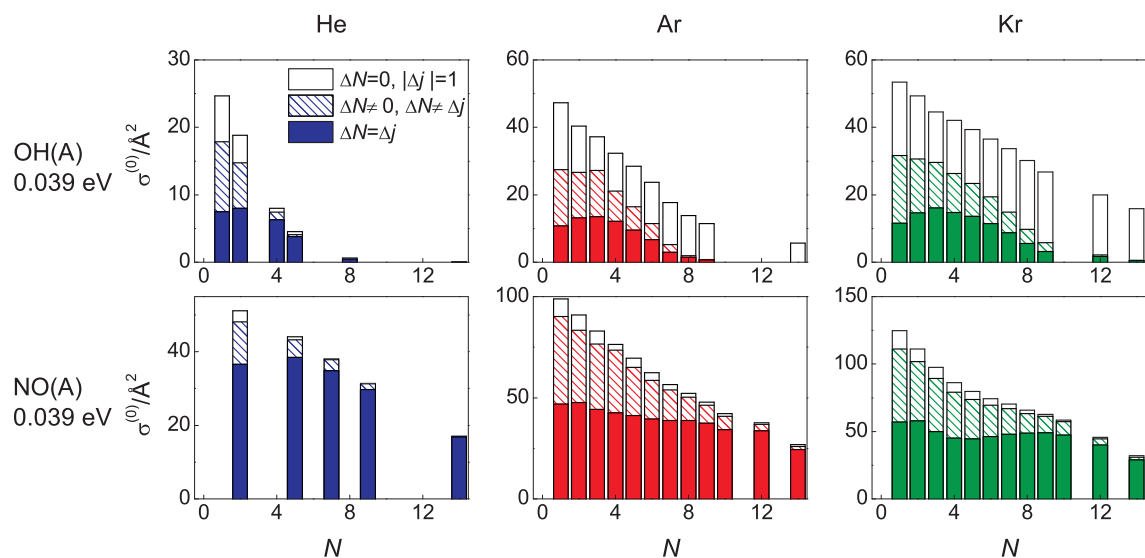


Figure 7. Fixed energy (0.039 eV) QCT total RET cross sections for OH(A) (top row) and NO(A) (bottom row) with He (left column), Ar (middle column) and Kr (right column). The total height of the bar shows the total RET cross-section, the top section of the bar to collisions which only change the spin-rotation level ( $N$  conserved but  $j$  changed), the middle section to collisions which change both  $N$  and the spin-rotation level, and the bottom section of the bar to collisions which change  $N$  but conserve the spin-rotation level. All the cross sections presented are for the  $f_2$  spin-rotation level.



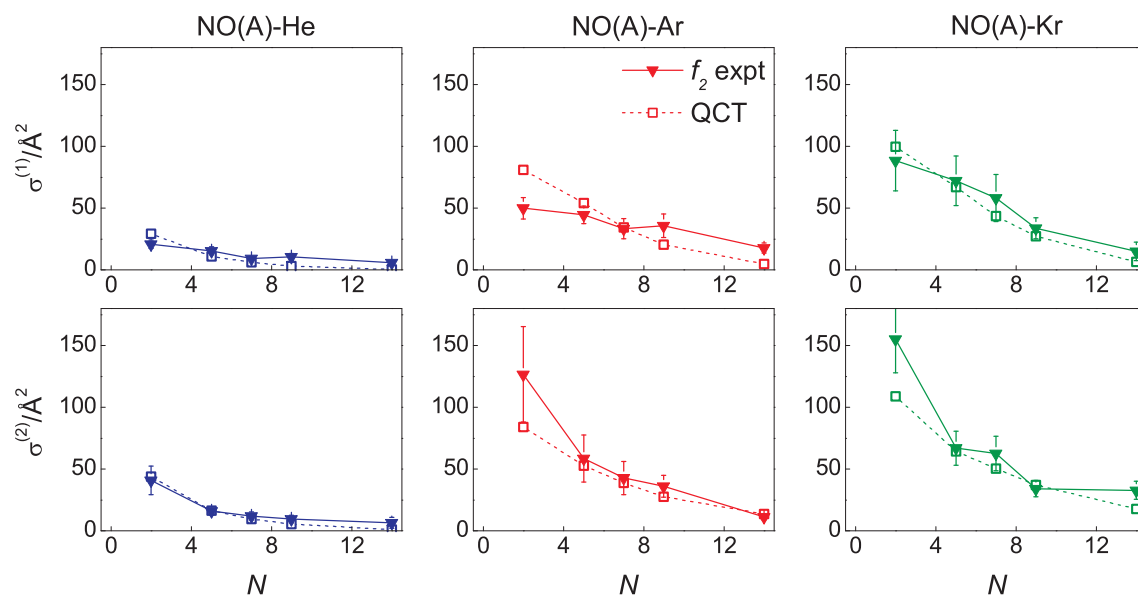


Figure 8. Comparison of the total (thermal, 300 K) disorientation (top row) and disalignment (bottom row) cross sections obtained experimentally (triangles) and from quasi-open shell fixed energy QCT calculations (0.039 eV, squares) for NO(A) + He (left panels), NO(A) + Ar (middle panels) and NO(A) + Kr (right panels). All the results presented are for the  $f_2$  spin-rotation level. The data are summed over all final rotational states ( $j' \neq j$ ), but are resolved in initial rotational state.

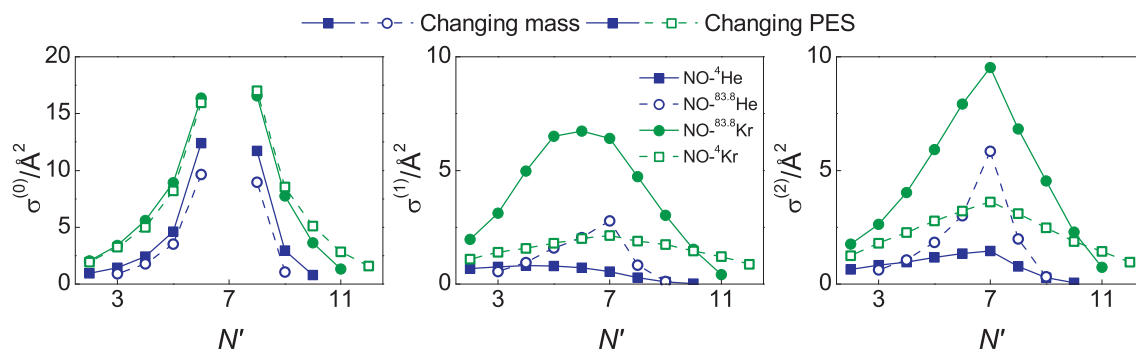


Figure 9. Comparison of the fixed energy (0.039 eV) QCT state-to-state RET (left panel), disorientation (middle panel) and disalignment (right panel) cross sections for  $N=7$  resolved in  $N'$ , showing the effect of the PES vs kinematics.

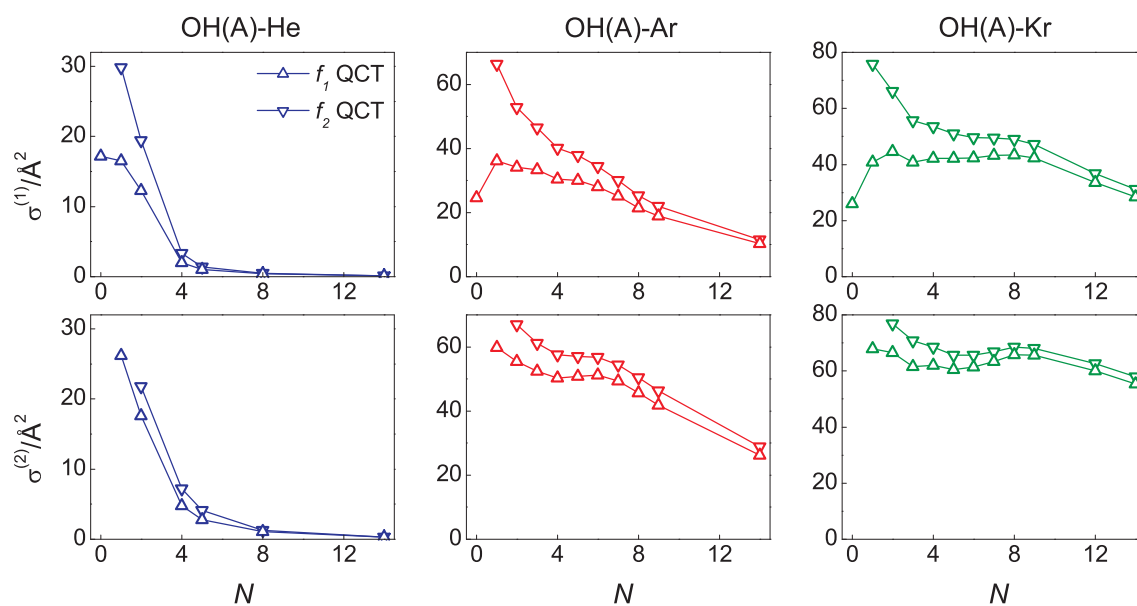


Figure 10. Total depolarisation cross sections for OH(A) + He (left panels), OH(A) + Ar (middle panels) and OH(A) + Kr (right panels) obtained for the  $f_1$  and  $f_2$  spin-rotation levels from the quasi-open shell fixed energy (0.039 eV) QCT calculations. The disorientation cross sections are presented in the top row, and the disalignment cross sections in the bottom row. The data are summed over all final rotational states ( $j' \neq j$ ), but are resolved in initial rotational state.

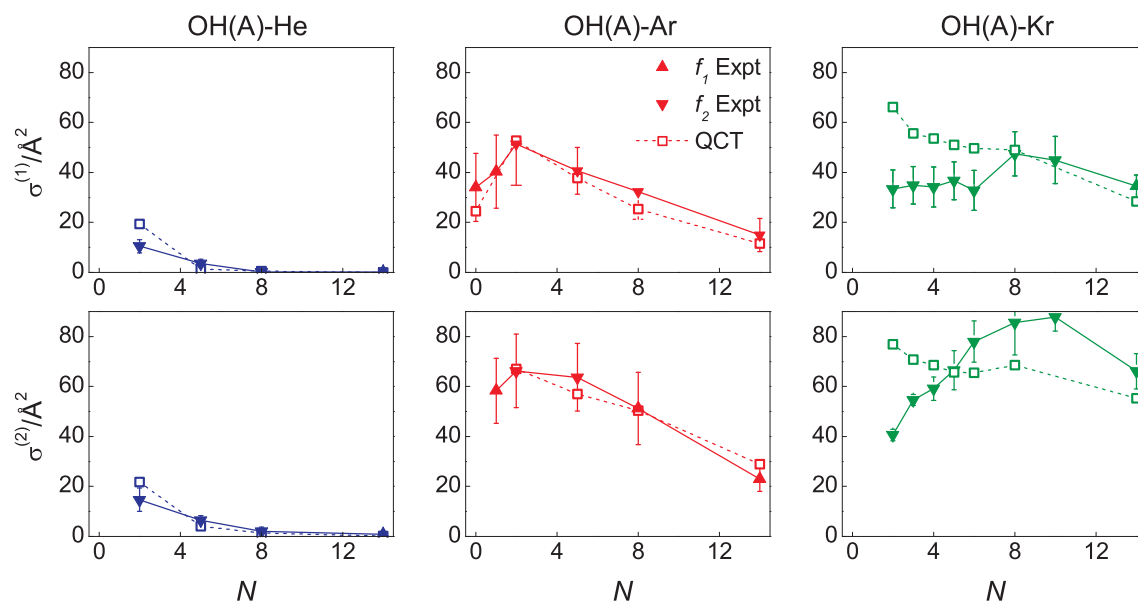


Figure 11. Comparison of the total thermal (300 K) disorientation (top row) and disalignment (bottom row) cross sections obtained experimentally (triangles) and from quasi-open shell fixed energy (0.039 eV) QCT calculations (squares) for OH(A) + He (left panels), OH(A) + Ar (middle panels) and OH(A) + Kr (right panels). The experimental results for the  $f_1$  levels are presented as upward pointing triangles, and those for the  $f_2$  levels as downwards pointing triangles. The results from the theoretical calculations are for the same spin-rotation level as observed experimentally. The data are summed over all final rotational states ( $j' \neq j$ ), but are resolved in initial rotational state.

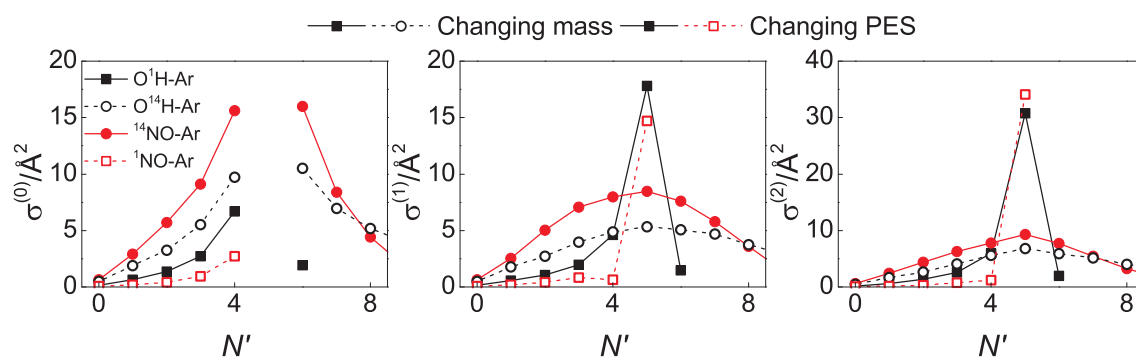


Figure 12. Comparison of the fixed energy (0.039 eV) QCT state-to-state RET (left panel), disorientation (middle panel) and disalignment (right panel) cross sections for  $N=5$  resolved in  $N'$ , showing the effect of the PES vs kinematics.

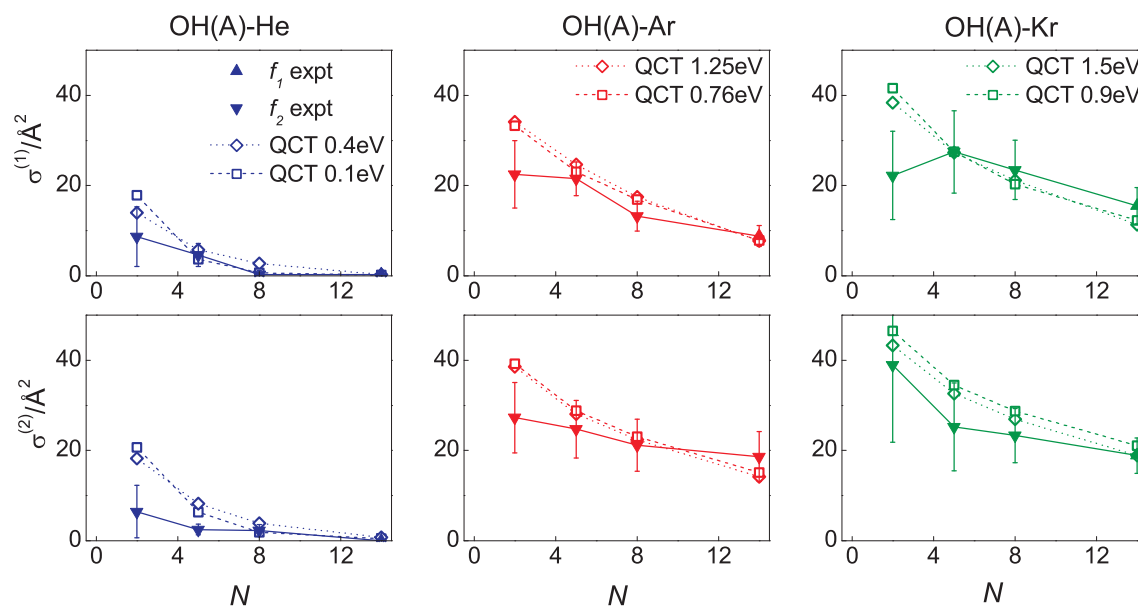


Figure 13. Comparison of the superthermal total disorientation (top row) and disalignment (bottom row) cross sections obtained experimentally (triangles) and from quasi-open shell QCT calculations (squares and diamonds) for OH(A) + He (left panels), OH(A) + Ar (middle panels) and OH(A) + Kr (right panels). The experimental results for the  $f_1$  levels are presented as upward pointing triangles, and those for the  $f_2$  levels as downwards pointing triangles. The results from the theoretical calculations are for the same spin-rotation level as observed experimentally, and are shown at two different fixed collision energies. The mean velocities used to convert the experimentally determined depolarisation rate constants to cross sections were  $2500 \text{ m s}^{-1}$  for OH(A) + He,  $3900 \text{ m s}^{-1}$  for OH(A) + Ar and  $3600 \text{ m s}^{-1}$  for OH(A) + Kr. The data are summed over all final rotational states ( $j' \neq j$ ), but are resolved in initial rotational state.

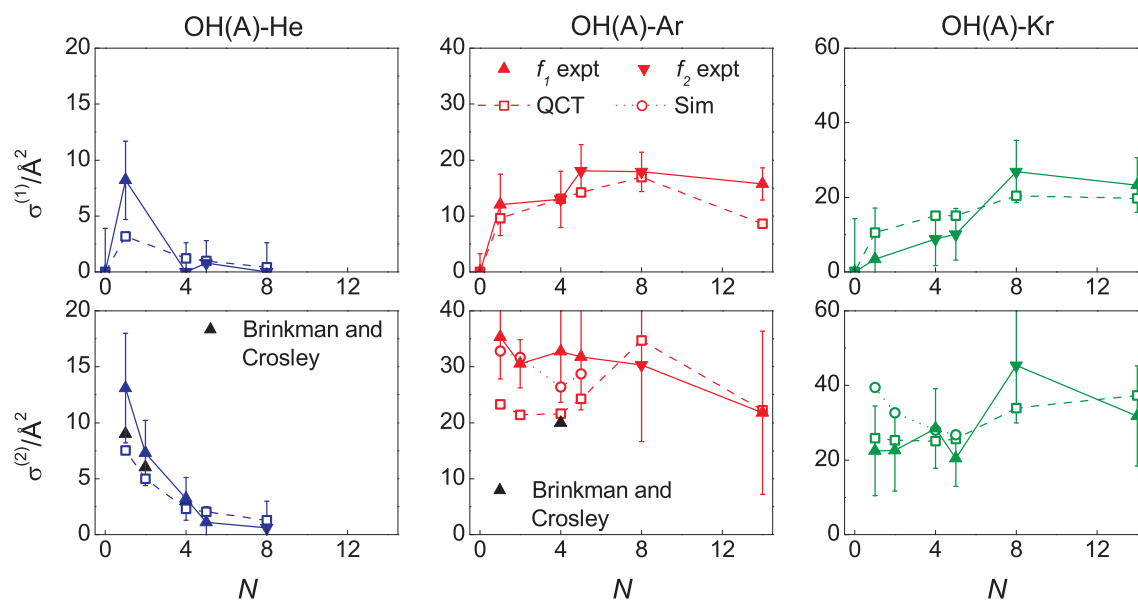


Figure 14. Thermal (300 K) elastic disorientation (top row) and disalignment (bottom row) cross sections for OH(A) + He (left column), OH(A) + Ar (middle column) and OH(A) + Kr (right column). The experimental results (triangles) are compared with the results from fixed energy (0.039 eV) QCT calculations (squares). Elastic disalignment cross sections from a previous study by Brinkman and Crosley [78] are shown for OH(A) + He and OH(A) + Ar as black triangles. The results from experimental simulations to determine the effects of overlapping satellites lines on the disalignment cross sections are also shown as open circles in the bottom panels for OH(A) + Ar and OH(A) + Kr. The experimental results for the  $f_1$  levels are presented as upward pointing triangles, and those for the  $f_2$  levels as downwards pointing triangles. The results from the theoretical calculations are for the same spin-rotation level as observed experimentally.

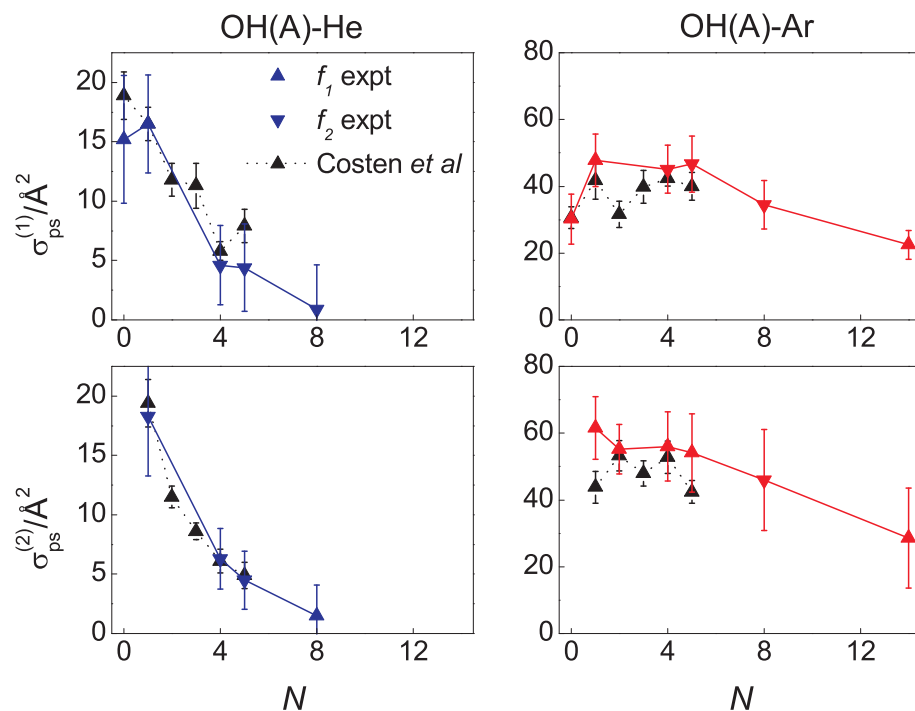


Figure 15. Comparison of the sum of the thermal (300 K) total RET and elastic disorientation cross sections (top panels) and sum of the (thermal) RET and disalignment cross sections (bottom panels) with the results obtained by Costen *et al.* [17] using two colour polarisation spectroscopy for OH(A) + He (left panels) and OH(A) + Ar (right panels). The experimental results for the  $f_1$  levels are presented as upward pointing triangles, and those for the  $f_2$  levels as downwards pointing triangles. The blue data in the left panel and the red data in the right panel are the Zeeman quantum beat results.



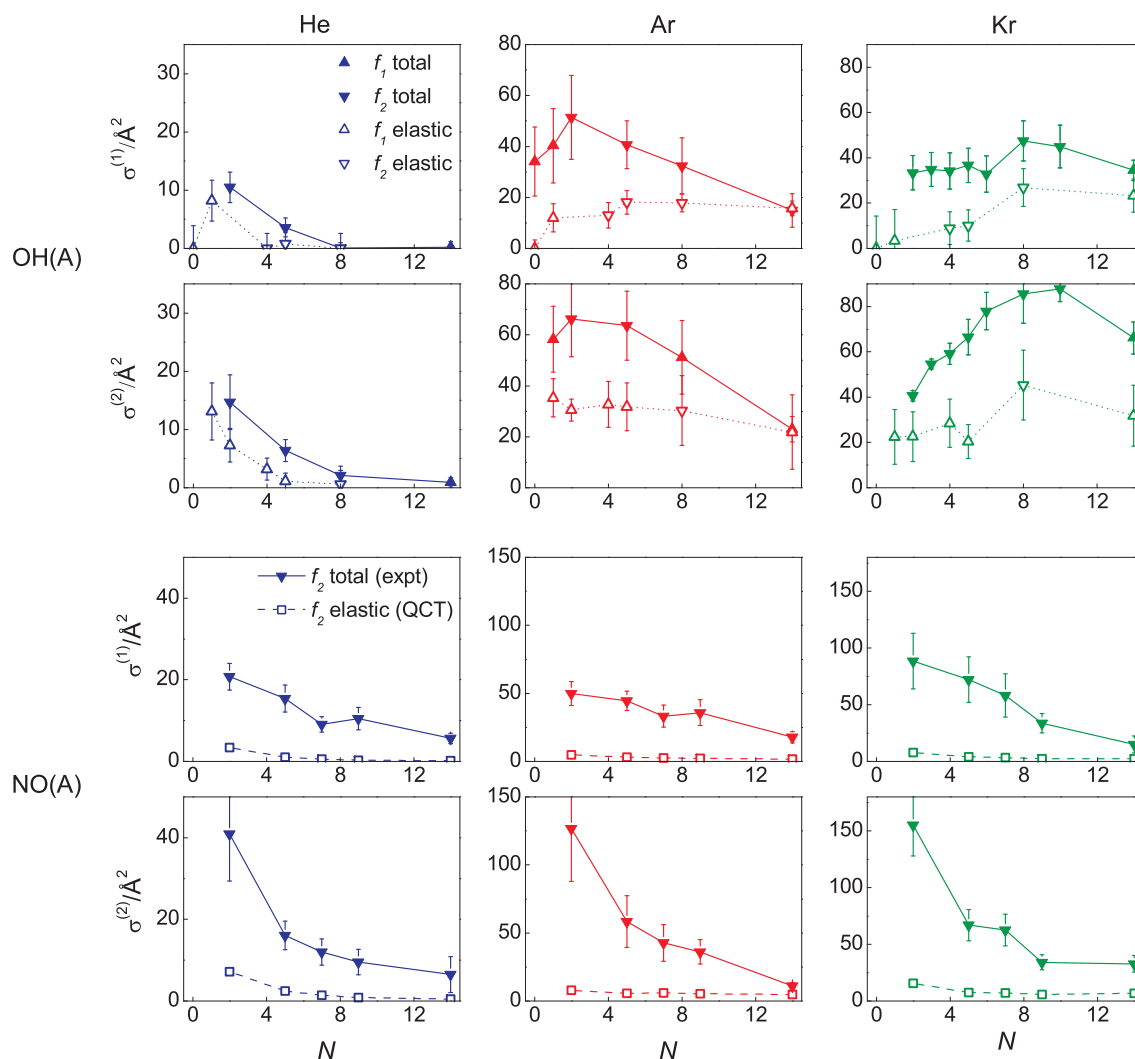


Figure 16. Comparison of the total depolarisation cross sections (filled triangles) with the elastic depolarisation cross sections (open triangles) measured experimentally under thermal conditions (300 K) for OH(A) (top two rows), and the total (thermal, 300 K) experimental (filled triangles) and theoretical elastic depolarisation cross sections (open squares) for NO(A) (bottom two rows). The top and third row correspond to disorientation, and the second and bottom row to disalignment. The left hand column presents the results for He, the middle for Ar and the right Kr. The experimental results for the  $f_1$  levels are presented as upward pointing triangles, and those for the  $f_2$  levels as downwards pointing triangles. The results from the theoretical calculations are for the same spin-rotation level as observed experimentally. The total depolarisation cross sections are summed over all final rotational states ( $j' \neq j$ ), but are resolved in initial rotational state.



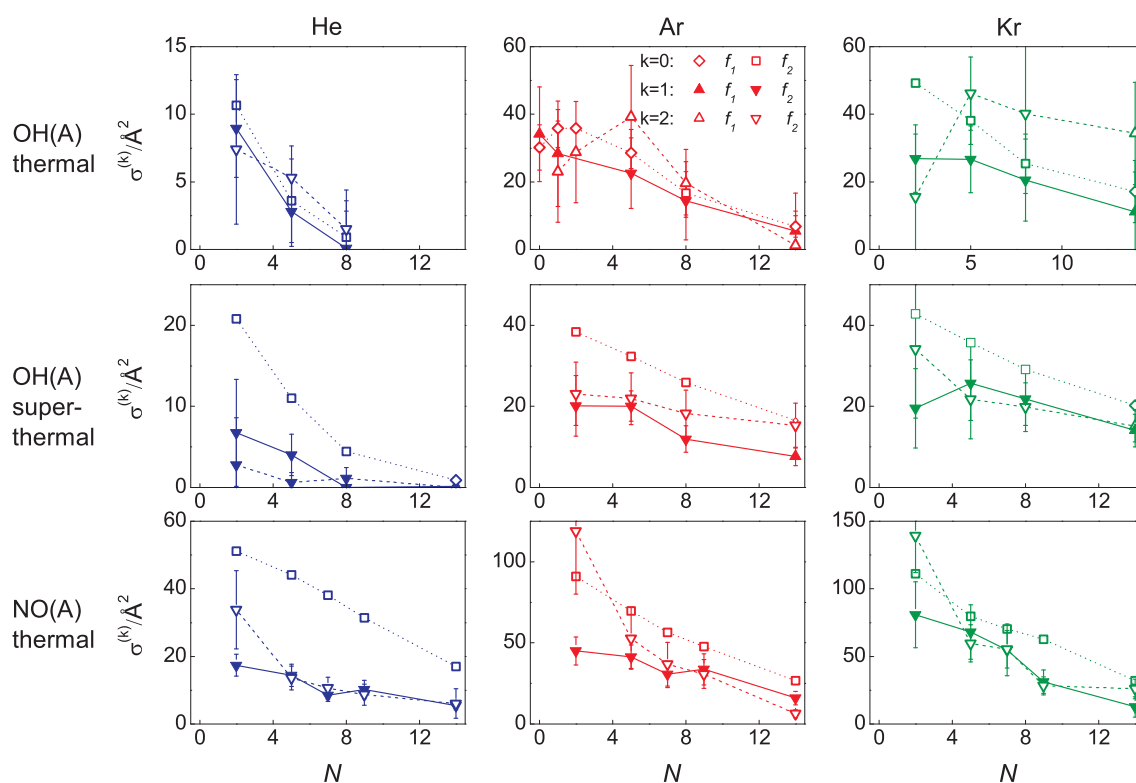


Figure 17. Comparison of the experimental total RET (open diamonds for  $f_1$ , open squares for  $f_2$ ) and inelastic depolarisation cross sections (triangles) for OH(A) under thermal conditions (300 K, top row), and the theoretical total RET (open diamonds for  $f_1$ , open squares for  $f_2$ ) and experimental inelastic depolarisation cross sections (triangles) for OH(A) under superthermal conditions (middle row) and NO(A) under thermal conditions (300 K, bottom row) for He (left column), Ar (middle column) and Kr (right column). The disorientation cross sections are shown as filled triangles, and the disalignment cross sections as open triangles. Experimental data has been used as far as possible, but where this is not available, QCT data has been used (fixed collision energy of 0.039 eV). The experimental results for the  $f_1$  levels are presented as upward pointing triangles, and those for the  $f_2$  levels as downwards pointing triangles. The theoretical RET data is obtained using Eq. 19 for  $\sigma_T^{(0)}$ .

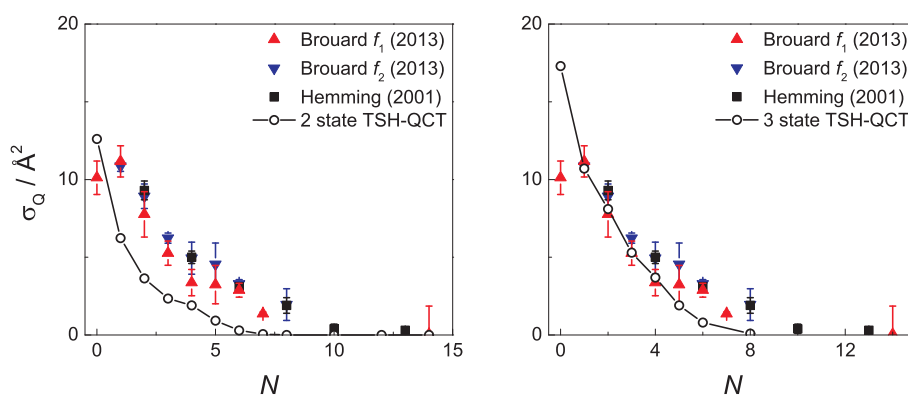


Figure 18. Electronic quenching cross sections for  $\text{OH}(A) + \text{Kr}$  resolved into the initial rotational state  $N$ . Experimental data (thermal, 300 K) [30]:  $f_1$  levels (red upward triangles),  $f_2$  levels (blue downward triangles). Black squares: Hemming *et al.* [65]. Trajectory surface-hopping QCT calculations (fixed energy, 0.039 eV) are shown with open circles, with the two state model [30] in the left hand panel and the three state model [27] on the right. Note that the spin-rotation level employed by Hemming *et al.* was not specified in their paper.

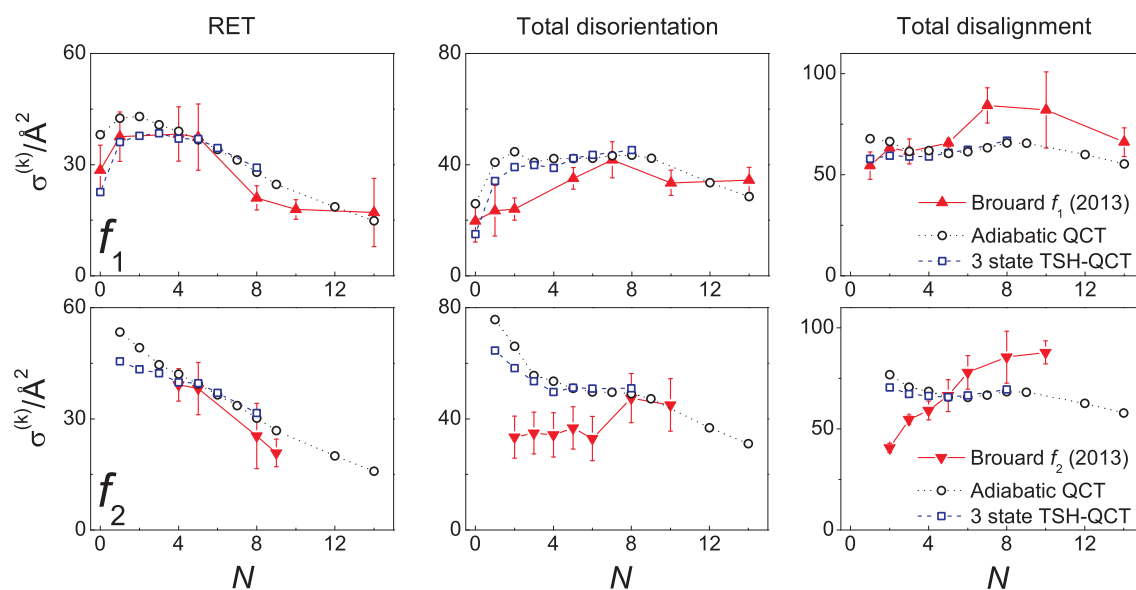


Figure 19. Comparison of experimental (thermal, 300 K) total RET (red triangles, left), total disorientation (red triangles, centre) and total disalignment (red triangles, right) to fixed energy (0.039 eV) adiabatic QCT (open circles) and fixed energy (0.039 eV) three state TSH-QCT (open squares) for OH(A) + Kr. Top row:  $f_1$  spin-rotation level, bottom row:  $f_2$  level. The data are summed over all final rotational states ( $j' \neq j$ ), but are resolved in initial rotational state. The theoretical RET data is obtained using Eq. 19 for  $\sigma_T^{(0)}$ .

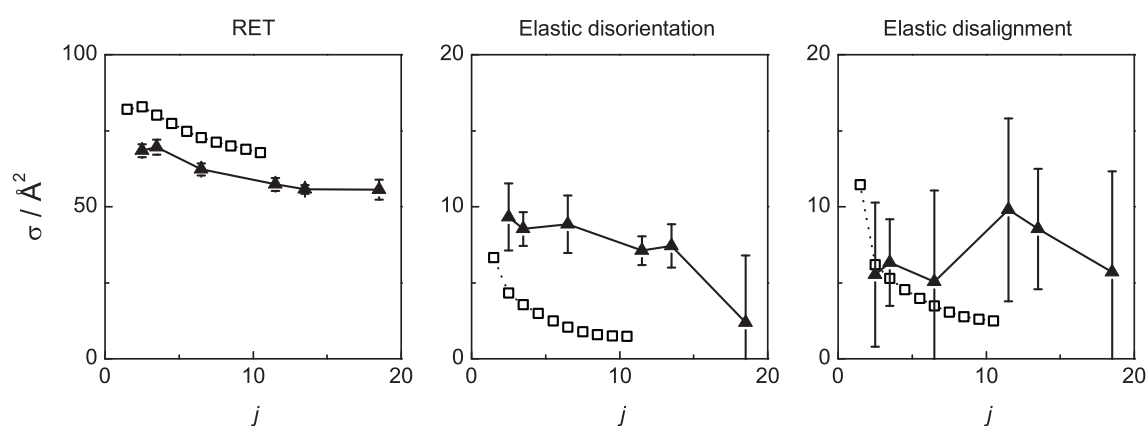


Figure 20. Experimental (thermal, 298 K, black triangles) and QM theoretical (thermally averaged, 298 K, open squares) cross sections for total RET (left), elastic disorientation (centre) and elastic disalignment (right) of  $\text{CN}(\text{A}, v = 4)$  by Ar. All data is taken from reference [25], and is for  $F_1e$  levels.

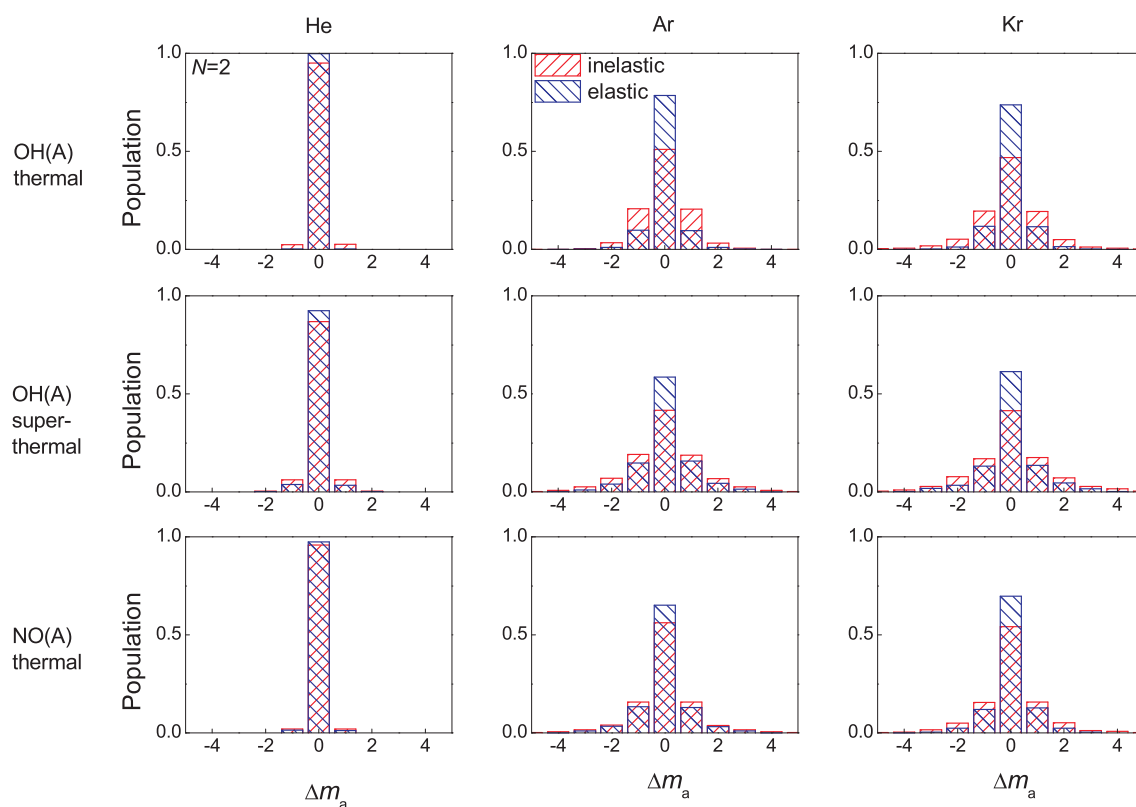


Figure 21. QCT (closed shell) histogram plots showing the change in the projection of  $\mathbf{j}$  onto the kinematic apse,  $\mathbf{a}$ ,  $\Delta m_a = m'_a - m_a$ , for OH(A) under thermal (300 K, top row) and superthermal (middle row) conditions, and NO(A) under thermal conditions (300 K, bottom row) in collisions with He (left column), Ar (middle column) and Kr (right column). Elastic depolarising trajectories ( $K \geq 0.5$ ) are shown in blue, and inelastic in red. The initial state in each case is  $N = 2$ , and the inelastic data are averaged over final state ( $N' \neq N$ ).

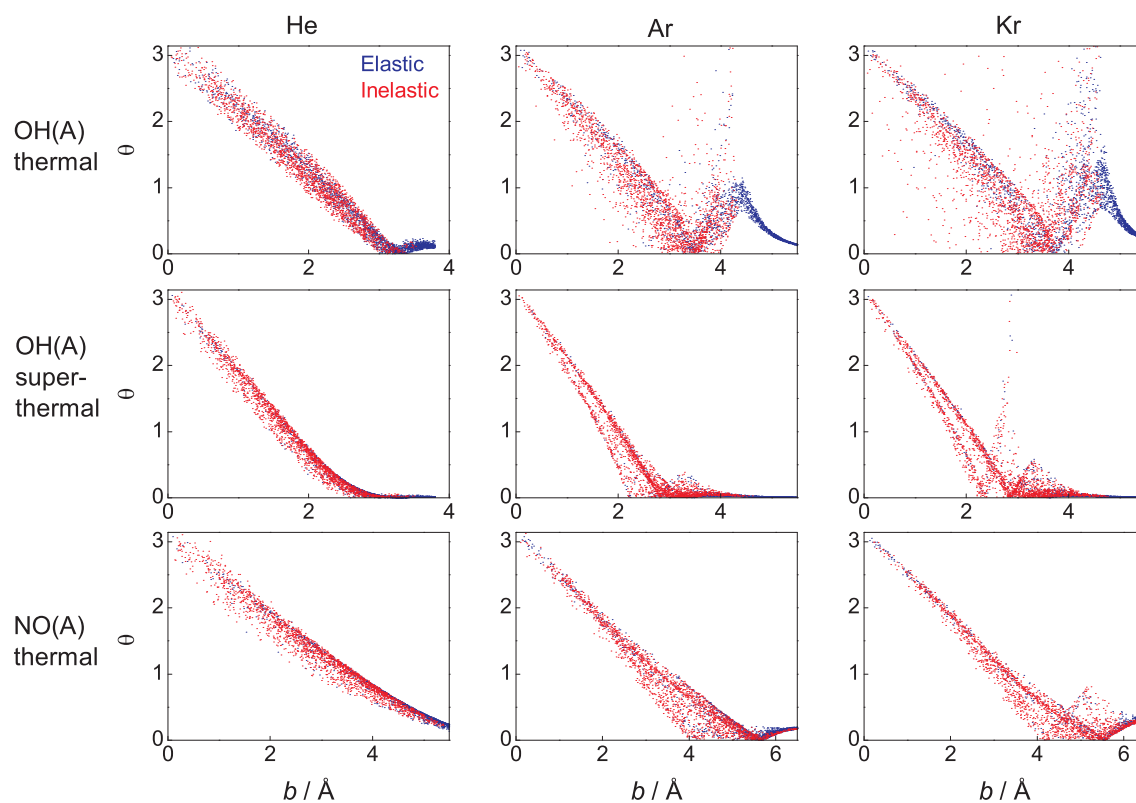


Figure 22. Closed shell QCT scatter plots of scattering angle versus impact parameter,  $b$ , for OH(A) under thermal (300 K, top row) and superthermal (middle row) conditions, and NO(A) under thermal conditions (300 K, bottom row) in collisions with He (left column), Ar (middle column) and Kr (right column). Elastic trajectories are shown in blue, and inelastic in red. The initial state in each case is  $N = 2$ , and the inelastic data are averaged over final state ( $N' \neq N$ ).



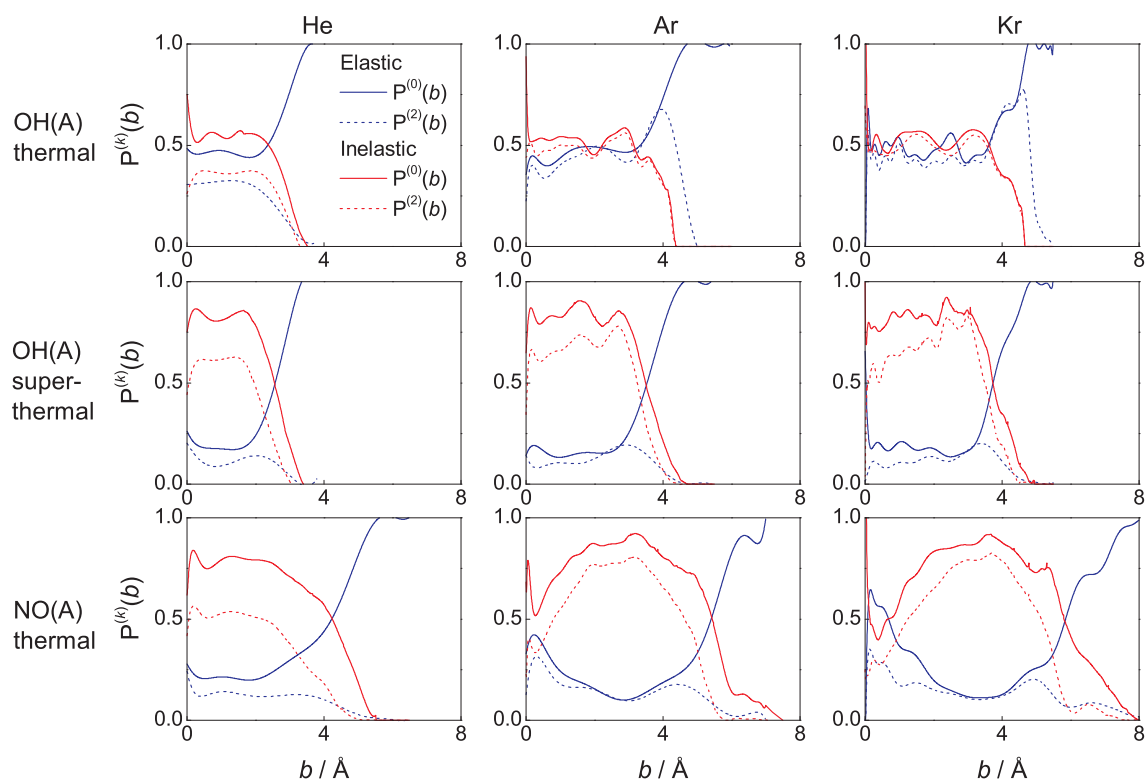


Figure 23. Closed shell QCT opacity functions for elastic (blue solid line) and inelastic (red solid line) collisions for thermal OH(A) (300 K, top row), superthermal OH(A) (middle row) and thermal NO(A) (300 K, bottom row) with He (left column), Ar (middle column) and Kr (right column). The dashed lines correspond to the disalignment opacity functions under the same conditions. The initial state in each case is  $N = 2$ , and the inelastic data are averaged over final state ( $N' \neq N$ ).

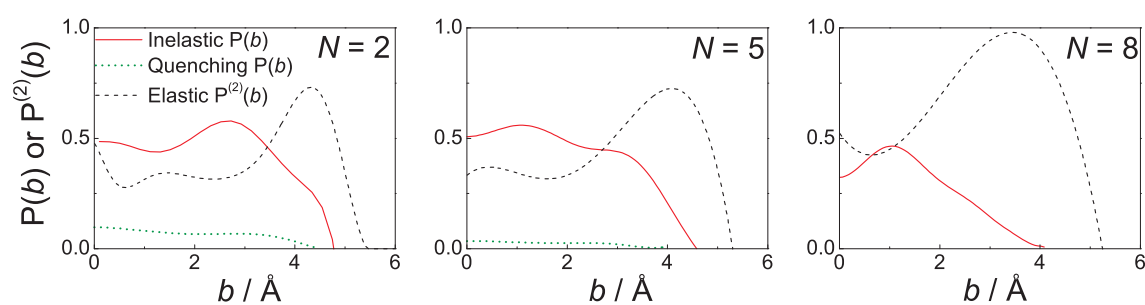


Figure 24. Closed shell QCT opacity functions for inelastic collisions (red solid line), elastic dis-aligning collisions (black dashed line) and electronic quenching (green dotted line) from two state fixed energy (0.039 eV) TSH-QCT for OH(A) + Kr. Left:  $N = 2$ , centre:  $N = 5$ , right:  $N = 8$ . Note that there is no surface-hopping at  $N = 8$ . The inelastic data are averaged over final state ( $N' \neq N$ ).

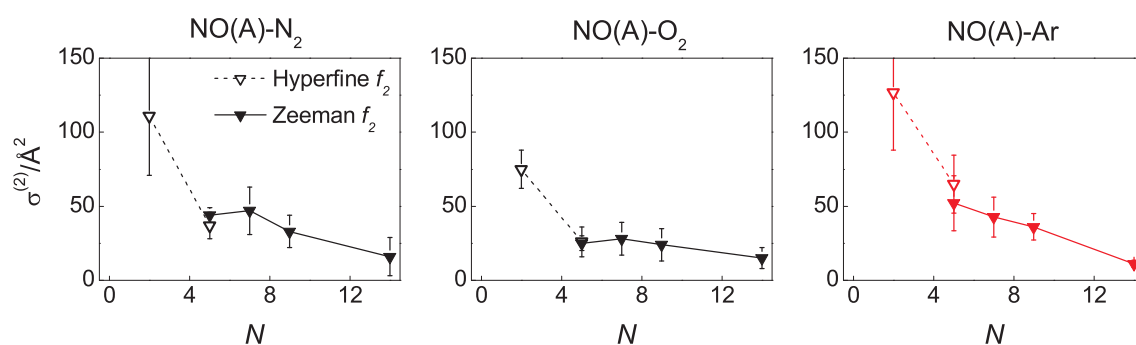


Figure 25. Total (thermal, 300 K) experimental disalignment cross sections for  $\text{NO(A)} + \text{N}_2$  (left panel) and  $\text{NO(A)} + \text{O}_2$  (middle panel), obtained using hyperfine quantum beat spectroscopy (open triangles) and Zeeman quantum beat spectroscopy (filled triangles). For ease of comparison, the  $\text{NO(A)} + \text{Ar}$  disalignment cross sections are shown in the right hand panel. All results are for the  $f_2$  spin-rotation level. The data are summed over all final rotational states ( $j' \neq j$ ), but are resolved in initial rotational state.

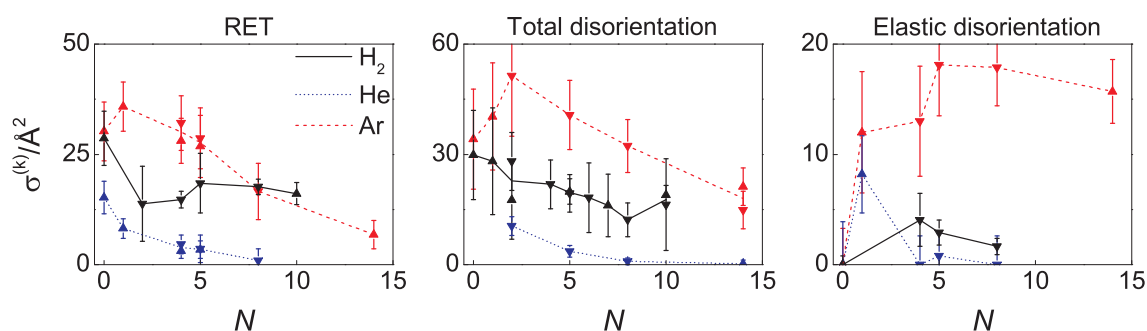


Figure 26. Thermally averaged (300 K) cross sections for RET (left panel), total disorientation (middle panel) and elastic disorientation (right panel) for  $\text{OH(A)} + \text{H}_2$  recorded experimentally (black solid line and triangles) and compared to results for  $\text{OH(A)} + \text{Ar}$  (red dashed line and triangles) and  $\text{OH(A)} + \text{He}$  (blue dotted line and triangles). The experimental results for the  $f_1$  spin-rotation level are presented as upward pointing triangles, and those for the  $f_2$  level as downwards pointing triangles. The data are summed over all final rotational states ( $j' \neq j$ ), but are resolved in initial rotational state.